



How reliable is distribution of relaxation times (DRT) analysis? A dual regression-classification perspective on DRT estimation, interpretation, and accuracy

Jake Huang ^{a,c,*}, Neal P. Sullivan ^b, Andriy Zakutayev ^c, Ryan O’Hayre ^a

^a Metallurgical and Materials Engineering, Colorado School of Mines, CO, USA

^b Mechanical Engineering, Colorado School of Mines, CO, USA

^c Materials Science Center, National Renewable Energy Laboratory, CO, USA



ARTICLE INFO

Keywords:

Electrochemical impedance spectroscopy
Distribution of relaxation times
Equivalent circuit
Autonomous
Classification

ABSTRACT

The distribution of relaxation times (DRT) has gained increasing attention and adoption in recent years as a versatile method for analyzing electrochemical impedance spectroscopy (EIS) data obtained from complex devices like fuel cells, electrolyzers, and batteries. The DRT deconvolutes the impedance without *a priori* specification of a generative model, which is especially useful for interpretation and model selection when the governing principles of the system under study are not fully understood. However, DRT estimation is an ill-posed inversion problem that must be addressed with a subjective choice of regularization and tuning, which leaves substantial risk of misleading interpretations of EIS data. In this work, we suggest a new classification view of the DRT inversion to clarify DRT estimation and interpretation. We introduce a dual regression-classification framework that unifies the classification and regression views of the DRT inversion with wide-reaching implications for DRT analysis. The dual framework is employed to demonstrate a new kind of DRT inversion algorithm and develop novel evaluation metrics that capture previously ignored aspects of DRT accuracy. These approaches are applied to both synthetic data and experimental spectra collected from a protonic ceramic fuel cell and a lithium-ion battery to illustrate their broad utility. The dual inversion algorithm shows promising performance for accurate DRT estimation and autonomous model identification, while the dual evaluation approach produces metrics that meaningfully assess the strengths and risks of DRT algorithms. This work provides valuable insight for both practical application of the DRT to experimental data and further development of EIS analysis methods.

1. Introduction

The distribution of relaxation times (DRT) has become increasingly popular in recent years as a technique for the analysis of electrochemical impedance spectroscopy (EIS) data. Unlike equivalent circuit models and physicochemical models, the DRT does not require the definition of discrete impedance contributions prior to analysis of the data. Instead, the impedance is assumed to arise from an infinite series of resistive-capacitive relaxations represented by a distribution function in the time domain (i.e. the DRT), typically represented as $\gamma(\ln \tau)$. The impedance of the distribution function is given by the fundamental relationship

$$z(\omega) = \int_{-\infty}^{\infty} \frac{\gamma(\ln \tau)}{1 + j\omega\tau} d \ln \tau, \quad (1)$$

which can be applied to directly estimate $\gamma(\ln \tau)$ from $z(\omega)$. Whereas physicochemical models and equivalent circuit models explicitly define the generative physical processes that produce the impedance, the DRT reveals the presence of these generative processes as characteristic peaks in the distribution [1–5]. Because the distribution can represent a wide variety of electrochemical behavior and emulate models of arbitrary complexity, the DRT is a versatile tool for model-free impedance deconvolution [1–4,6–8]. Since the DRT is typically employed when knowledge of the system under study is incomplete, DRT estimates are often used to identify and quantify discrete impedance contributions, assign physical meaning to different features of the impedance spectrum, and/or inform physical or equivalent circuit models [1–5].

Nonetheless, the DRT faces its own challenges: estimating the DRT from noisy impedance data is an ill-posed inversion problem, meaning

* Corresponding author at: Metallurgical and Materials Engineering, Colorado School of Mines, CO, USA.

E-mail address: jduhuang@mines.edu (J. Huang).

URL: <https://github.com/jduhuang-csm> (J. Huang).

that many different distributions can yield nearly identical impedance spectra. In order to resolve the ambiguity of the inversion problem, the principle of parsimony must be applied [8–12]: all else being equal, the simplest solution that describes the data appropriately is taken to be the most credible solution. Numerous approaches to implementing the principle of parsimony in the DRT inversion have been developed, including entropy maximization [13], Fourier transform methods [14], Bayesian regression [9,10,15–19], and neural networks [20]. Despite this diversity, virtually all existing DRT algorithms formulate the DRT inversion as a regression problem: the objective is to predict the magnitude of γ as a continuous function of $\ln \tau$ as accurately as possible. However, this view discards the crucial information that the DRT represents a discrete set of generative processes. As a result, interpreting the results of these algorithms is difficult: erroneous peaks and/or peak omissions are easily produced, yielding misleading interpretations of the data. This highlights a fundamental mismatch between standard approaches to DRT estimation and DRT interpretation: DRT inversion algorithms are focused on regression, but our end use of the DRT is more akin to classification.

To better align the foundations of DRT analysis with our physical understanding of impedance, we suggest that DRT estimation may be viewed as a classification problem. In this view, the objective is to identify the discrete relaxations that generated the impedance. A few approaches proposed in the literature have partially broached this concept. Some authors have proposed constructing the DRT from a small number of basis elements, consecutively adding elements until a desired goodness of fit is achieved [8,14]. However, these approaches are more similar in nature to equivalent circuit analogs than conventional DRT algorithms and face the challenges characteristic of such models: ambiguity of model selection, risk of parameter non-convergence, and higher computational cost [18,21]. In addition, shape mismatches between the basis elements and the true relaxations can result in models lacking clear physical meaning [21]. Another study proposed an algorithm to automatically identify peaks in a conventional DRT estimate and construct an equivalent circuit accordingly [5]. Because this method treats the DRT estimate as ground truth, it suffers from the same problems and risks as conventional regression-based DRT algorithms. Neither type of approach fully accounts for uncertainty in model selection.

In this work, we introduce a framework that unifies the regression and classification views by recognizing that the DRT is simultaneously a continuous distribution and a discrete set of relaxations. A central tenet of the framework is that uncertainty, which is inevitable in EIS data, must be reflected in DRT analysis. The dual nature of the DRT motivates a new class of inversion algorithms that leverage both continuous and discrete representations of the DRT to address both the regression and classification objectives of DRT estimation. We demonstrate an exemplary algorithm that employs the continuous representation to efficiently explore the solution space and identify *candidate* relaxations. This enables the construction of a novel *probability function* of relaxation times (PFRT), which is the classification-centric analog of the regression-centric DRT. The classification view allows us to directly predict the presence of particular relaxations and quantify their credibility, providing new insight into the uncertainty inherent in the DRT. The candidate relaxations yield a set of candidate discrete models and corresponding plausibilities that represent different generative models of the data. This dual inversion framework establishes an autonomous approach to model construction, improves the interpretability and accuracy of the resulting models, enables separation and quantification of distinct physical relaxations, and directly connects continuous and discrete models.

The dual regression-classification perspective also has important implications for understanding the accuracy of DRT algorithms. We show that evaluation metrics derived from regression and classification views of the DRT inversion problem quantify fundamentally different aspects of DRT accuracy. We demonstrate that both views are necessary to fully describe the accuracy of DRT algorithms and propose fully

descriptive hybrid metrics. The metrics developed in this work are useful for benchmarking DRT algorithms, informing how DRT estimates are interpreted in practice, and developing and validating new DRT estimation techniques. The dual regression-classification framework also provides conceptual and mathematical foundations for further development of methods for assessing DRT accuracy.

The text is structured to provide value to DRT theorists and end users alike. The main text gives an accessible overview and demonstration of the dual regression-classification perspective, while the rigorous mathematical and algorithmic foundations underlying the framework are developed in the supplementary information. A Python implementation of the methods described here is provided for use and development at github.com/jdhuang-csm/hybrid-drt.

2. Methods

The dual regression-classification framework is motivated by the expectation that the DRT arises from a discrete set of physical processes (relaxations), each of which has a characteristic distribution function. The framework is based on several assumptions:

1. The exact DRT can be represented as a sum of discrete relaxation distribution functions.
2. Each relaxation distribution function contains a single peak.
3. All else being equal, DRTs comprising fewer discrete relaxations are more credible.

We provide further detail and caveats for these assumptions. Assumption 1 encapsulates the understanding that the DRT represents a finite set of discrete physical processes and allows for inter-conversion between continuous and discrete representations. Assumption 2 requires a precise definition of what constitutes a “peak”. We define a peak as a local minimum in curvature, rather than a local maximum in the distribution, to ensure that shoulder peaks are captured by the definition [5,22,23]. Assumption 2 is valid for most common electrochemical processes and equivalent circuit elements, including RC, ZARC, Gerischer, and Havriliak–Negami elements [6,9]. However, this is not guaranteed to hold for all types of relaxations. For example, the equivalent DRT of the fractal Warburg consists of an infinite number of peaks [24]. In the case of generative processes with multimodal distribution functions, the framework can still be applied — the multimodal relaxation will simply be considered more complex than a unimodal relaxation. However, one should also consider whether the DRT is suitable to model such a relaxation. In the case of the fractal Warburg, a constant phase element [25] or a distribution of diffusion times [26] might be more appropriate than the DRT. No further assumptions beyond unimodality are made about the shape (dispersion, asymmetry, etc.) of the relaxation distribution function. Assumption 3 provides the core definition of model complexity that allows us to apply the principle of parsimony to resolve the ill-posed inversion problem. These assumptions do not result in any loss of generality: any system that can be treated with the conventional DRT can also be treated within the dual framework.

The following sections develop the conceptual foundations of the framework from this central philosophy. We focus on describing the concepts and application of the dual framework in the main text and relegate most mathematical details to the appendices. Section 2.1 provides a general approach to harness duality in DRT estimation and describes one possible algorithm. Section 2.2 explains the regression and classification views of DRT accuracy and defines corresponding evaluation metrics. Section 2.3 describes the simulated and experimental data employed to demonstrate the framework.

Matrix and vector notation. In this work, we use bold lowercase letters to indicate vectors, bold uppercase letters to indicate matrices, and subscripts to indicate indexed elements of vectors and matrices, as illustrated below:

v	Vector
M	Matrix
v_i or $(\mathbf{v})_i$	Entry i of vector v
m_{ij} or $(\mathbf{M})_{ij}$	Entry in row i , column j of matrix M

The unbolted indexed notation (v_i, m_{ij}) is used when the vector or matrix is represented by a single character, whereas the bolded parenthetical notation $((\mathbf{v})_i, (\mathbf{M})_{ij})$ is used when the vector or matrix contains a subscript. For example, the i th element of a vector **a** would be written a_i , whereas the i th element of a vector \mathbf{a}_b would be written $(\mathbf{a}_b)_i$.

2.1. DRT inversion

The DRT inversion problem is concerned with estimating the exact DRT, $\gamma_{\text{exact}}(\ln \tau)$, from impedance data. In the regression view, the objective is to determine the magnitude of γ_{exact} as a function of $\ln \tau$, while the classification objective is to identify the discrete relaxations that comprise $\gamma_{\text{exact}}(\ln \tau)$. For either objective, we must choose how to represent the model DRT, $\gamma_{\text{model}}(\ln \tau)$. We may choose a continuous representation, most often a linear combination of radial basis functions on a fixed $\ln \tau$ grid [27], in which the model DRT is a function of $\ln \tau$ without any explicit discrete structure. The solution is typically regularized, or constrained, by applying a smoothing penalty to the slope or curvature of the model DRT [9,10,15,16,18,28]. Alternatively, we may select a discrete representation, in which the model DRT is a finite series of basis elements, such as equivalent circuit elements, each of which describes a particular feature of the impedance. While both representations may involve basis elements or functions, the continuous representation uses a large number of elements with fixed time constants and shape (fixed basis), whereas the discrete representation uses a small number of elements and optimizes their time constants and shapes (floating basis) [8]. The continuous representation enables computationally efficient, model-free solutions to the regression problem. However, it cannot directly constrain the number of peaks that appear: because distribution *sharpness/smoothness* is an imperfect proxy for the *presence/absence of peaks* (discrete relaxations), continuous DRT estimates can easily produce false peaks or omit true relaxation processes. The discrete representation supplies an explicit constraint on the number of relaxations, but requires a predetermined model. Discrete models also rely on slower nonlinear optimization algorithms and require suitable parameter estimates for reliable convergence.

The dual framework seeks to take advantage of both representations to simultaneously achieve the regression and classification objectives. The core operating principle of the dual inversion framework is that *the continuous representation guides us to possible discrete models*, while *the discrete representation allows us to directly test those models*. The continuous representation is poorly suited to the latter task because the number of peaks can only be indirectly controlled via smoothing regularization, whereas the discrete representation is poorly suited to the former task because it requires guessing (or obtaining by brute force) suitable models and parameter values. The resulting *candidate* discrete models represent different possible explanations of the data, which can then be evaluated and compared. The classification and regression objectives are both satisfied by the generation of these candidate discrete models.

The following sections describe an approach for applying this principle, illustrated schematically in Fig. 1. Section 2.1.2 provides an algorithm for identifying candidate models by applying the continuous representation. Section 2.1.3 describes how candidates identified by the continuous representation may be efficiently converted to optimized

discrete models. Section 2.1.4 then explains how the candidates describe a probability function of relaxation times and provides criteria for comparison and selection of the most suitable model(s) from the resulting candidate discrete models. Throughout, a Bayesian view is employed to balance the data with model complexity. The final output of this dual inversion algorithm is a set of possible models and corresponding probabilities. We stress that this is just one possible implementation of the philosophy underlying the dual framework: the framework provides a conceptual structure for approaching EIS analysis but does not prescribe details of the algorithm.

2.1.1. Problem setting

Consider an EIS measurement over a vector of N frequencies, $\omega \in \mathbb{R}^N$, which produces a complex vector of measured impedance values, $\mathbf{z}'_{\text{exp}} + j\mathbf{z}''_{\text{exp}}$, where $\mathbf{z}'_{\text{exp}} \in \mathbb{R}^N$, $\mathbf{z}''_{\text{exp}} \in \mathbb{R}^N$, and j is the imaginary unit. For convenience, we define the concatenated experimental impedance vector, $\mathbf{z}_{\text{exp}} \in \mathbb{R}^{2N}$, as the concatenation of the real and imaginary impedance vectors:

$$\mathbf{z}_{\text{exp}} = \begin{bmatrix} \mathbf{z}'_{\text{exp}} \\ \mathbf{z}''_{\text{exp}} \end{bmatrix} \quad (2)$$

Given this data, our objective is to estimate the true DRT responsible for generating the impedance, γ_{exact} , and identify its constituent relaxations. The dual framework approaches this using a continuous model of the DRT, γ_{cont} , in concert with a discrete model of the DRT, γ_{disc} .

2.1.2. Candidate model identification

We exploit the efficiency and versatility of the continuous DRT representation to identify possible discrete models for the data. The continuous DRT is represented as a linear combination of M radial basis functions (RBFs),

$$\gamma_{\text{cont}}(\ln \tau) = \sum_{m=1}^M x_m \phi_m(\ln \tau), \quad (3)$$

where $\phi_m(\ln \tau)$ is an RBF centered at $\ln \tau = \ln \tau_m$ and x_m is its magnitude. The continuous representation results in a linear model (see Section S1.1 for details):

$$\mathbf{z}_{\text{exp}} = \mathbf{A}\mathbf{x} + \boldsymbol{\epsilon}_{\text{cont}}, \quad (4)$$

where $\mathbf{A} \in \mathbb{R}^{2N \times M}$ is the impedance evaluation matrix, $\mathbf{x} \in \mathbb{R}^M$ is the vector of RBF magnitudes that determines γ_{cont} , and $\boldsymbol{\epsilon}_{\text{cont}} \in \mathbb{R}^{2N}$ is the concatenated vector of real and imaginary impedance residuals. Regularization must be applied to γ_{cont} to obtain meaningful solutions for \mathbf{x} . However, the strength of the regularization is controlled by one or more *hyperparameters* which have a strong influence on the solution and must be tuned appropriately. The uncertainty in tuning the hyperparameter values is a central challenge in the design of continuous DRT algorithms, and although several methods have been proposed to identify optimal values [8–11,17,18,29], no tuning method is guaranteed to produce an accurate DRT estimate. Instead, the dual framework recognizes and utilizes this uncertainty: varying the tuning hyperparameters produces different *candidate* solutions that vary in complexity. The key principle underlying the usefulness of the candidates is that *peaks that remain in the solution under stronger regularization are more credible* than those which appear only at lower regularization levels. Conceptually, we can start from a strongly regularized solution containing only one peak and then gradually decrease the regularization level, revealing incrementally more complex solutions as new peaks appear. Each candidate identified in this way represents a different balance between the data and our prior beliefs: simpler models give more weight to parsimony, while complex models give more weight to the data.

In general, any continuous DRT algorithm can be applied to generate candidate solutions by performing two steps: (1) adjust the tuning hyperparameters to obtain solutions of varying complexity, and (2)

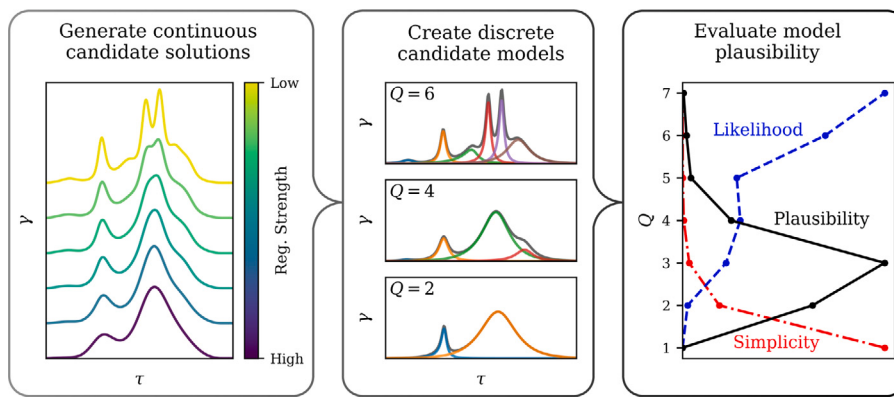


Fig. 1. Schematic illustration of the dual inversion algorithm. First, candidate solutions are generated by varying the regularization strength of the continuous DRT algorithm. Next, the continuous candidates are used to identify and optimize discrete model analogs with different numbers of elements (Q). Finally, the discrete models are evaluated by considering their simplicity and likelihood (data fit quality), which together determine the overall model plausibility for each possible set of elements Q . The models with the highest plausibility represent the most probable explanations of the data.

identify peaks in the candidate solutions. The first step is model-dependent, but generic methods can be used for the second step. To demonstrate the procedure, we employ a hierarchical ridge regression model and develop a method for systematically adjusting the tuning hyperparameters to obtain candidate solutions. We then provide a simple algorithm for determining the complexity of each solution and selecting representative candidates. Each component of the procedure is outlined below.

Hierarchical ridge regression model. While any continuous DRT inversion algorithm can be used for candidate generation, algorithms that are fast and reliably suppress false peaks are best suited to this use case. We employ a hierarchical ridge regression model based on previous works by Ciucci and Chen [10] and Huang, Papac, and O'Hare [18]. Our hierarchical ridge model takes key features from the hierarchical prior structure developed in [18], which imposes penalties on the magnitude, slope, and curvature of the DRT to effectively suppress pseudo-peaks, estimates the non-uniform error structure of the data, and uses Bayesian inference to tune many hyperparameters. To ensure computational efficiency and convergence, the model is optimized using the iterative quadratic programming method developed in [10], rather than the non-linear optimization procedure applied in [18]. Since the continuous DRT algorithm is not the focus of this work and the ridge regression approach to DRT inversion has been thoroughly examined in the literature, we provide an abbreviated definition of our model in Section S1.

Variation of hyperparameters. The tuning hyperparameters of the hierarchical ridge model are systematically varied to generate candidate solutions. We start from a default set of hyperparameter values that generally produces a well-tuned baseline solution, summarized in Section S1.9, which was determined empirically following a calibration procedure similar to that described in [18]. To obtain candidate solutions simpler than the baseline solution, the effective regularization strength is incrementally increased in steps, and the solution algorithm is applied at each step until convergence. Because the solution algorithm is iterative, this procedure generates a series of solutions, each of which is a continuous candidate that may be considered in later steps. To obtain more complex solutions, a similar procedure is applied to gradually decrease the effective regularization strength, producing a series of candidate solutions of increasing complexity. The details of the hyperparameter adjustments for candidate generation are given in Section S1.10.

Complexity determination. Once candidate distributions have been generated, a peak-finding algorithm is applied to determine the complexity of each solution. To ensure that both primary and shoulder peaks are reliably identified, we use local minima in the curvature of γ_{cont} to

identify peaks [5,22,23]. Each local minimum in the curvature is considered to represent a peak if (1) the curvature is negative and (2) the topographic prominence [30,31] of the peak exceeds a threshold. The prominence threshold is set to $0.005R_p + 0.05 \text{ std}(d^2\gamma/d\ln\tau^2)$, where R_p is the polarization resistance and $\text{std}(x)$ is the standard deviation of x , to ensure that peaks that are significant relative to the baseline level of curvature variation are captured. Our choice of peak identification algorithm is not intended to be definitive: the procedures defined in this section can easily be performed with any peak identification method. We use the approach described above as a simple and interpretable starting point, but other peak-finding methods should be examined.

After peaks have been identified in all candidate distributions, the candidates are grouped by the number of identified peaks, Q . Within each group, the best candidate is chosen to be that which provides the best explanation of the data as quantified by the log-likelihood function, $\ln \mathcal{L}(x)$ (Equation S51), which accounts for the impedance errors (residuals) and data weighting. This process produces a set of representative continuous candidate solutions, each containing a different number of peaks. These representatives provide the basis for considering a corresponding set of discrete element models.

In some cases, a candidate of the desired complexity may not be identified. For example, it is possible that candidates with either two peaks or four peaks are identified without the generation of a candidate with three peaks. In such cases, the missing candidate(s) can easily be produced by removing the lowest-prominence peak(s) in the more complex model. In the above example with two-peak and four-peak candidates, the peak with the smallest prominence in the four-peak candidate would be ignored to produce a new candidate with three peaks. This procedure ensures that candidates of incrementally increasing complexity can be identified even in cases in which multiple peaks appear in concert in the continuous DRT estimates.

2.1.3. Continuous to discrete model conversion

The continuous candidate solutions can be interpreted as discrete models via peak identification. However, the conversion of the continuous candidates to parameterized discrete element models is desirable for two main reasons. First, the number of identified peaks is inherently coupled to peak sharpness in the DRT candidates due to the use of smoothing priors: continuous candidates with fewer peaks will also tend to have broader peaks, which may inflate the apparent error, as shown in Section 3.1. Second, the continuous candidates do not provide descriptive parameters for peak size or shape. Explicit conversion of the continuous candidates to discrete element models addresses both of these issues.

We construct each discrete element model by defining a circuit analog consisting of an ohmic resistance and an inductance in series

with Q basis elements, each of which represents a peak in the continuous DRT. The nature of the basis elements is important to both the fitting and interpretation of the discrete model: a basis element that cannot describe the shape of the true relaxation distribution will fit the data poorly, may lead to selection of an incorrect model, and provides misleading information about the nature of the relaxation. In order to describe a wide variety of peak shapes anticipated by theory and empirical findings, we parameterize each peak with a Havriliak-Negami (HN) element, but other basis elements could be employed. The HN element is a generalization of ZARC and Gerischer elements that is capable of describing peaks that vary both in dispersion and symmetry [6]. The exact DRT of the HN element is given by

$$\gamma_{\text{HN}}(\ln \tau) = \frac{R}{\pi} \frac{(\tau/\tau_0)^{\alpha\beta} \sin(\alpha\theta_{\text{HN}})}{(1 + 2 \cos(\pi\beta)(\tau/\tau_0)^\beta + (\tau/\tau_0)^{2\beta})^{\alpha/2}}, \quad (5)$$

where R , τ_0 , α , and β are the resistance, characteristic time constant, symmetry parameter, and dispersion parameter, respectively, and θ_{HN} is given by

$$\theta_{\text{HN}}(\ln \tau) = \tan^{-1} \left(\frac{\sin(\pi\beta)}{(\tau/\tau_0)^\beta + \cos(\pi\beta)} \right). \quad (6)$$

The impedance of the HN element is given by

$$z_{\text{HN}}(\omega) = \frac{R}{(1 + (j\omega\tau_0)^\beta)^\alpha}. \quad (7)$$

Both α and β range from 0 to 1. When $\alpha < 1$, the HN DRT peak is asymmetric with a longer tail on the left side. The degree of asymmetry increases as α decreases, while the degree of dispersion increases as β decreases. Special cases of the shape parameters correspond to simpler circuit analogs: when $\alpha = \beta = 1$, the HN element reduces to the RC element; when $\alpha = 1$, the HN element reduces to the ZARC element; when $\alpha = 0.5$ and $\beta = 1$, the HN element reduces to the Gerischer element. The discrete model DRT is then defined by the sum of its constituent relaxation distribution functions,

$$\gamma_{\text{disc}}(\ln \tau) = \sum_{q=1}^Q \gamma_{\text{HN},q}(\ln \tau), \quad (8)$$

where $\gamma_{\text{HN},q}(\ln \tau)$ is the DRT of the q th HN element.

The HN element enables the construction of versatile discrete models, each of which produces a non-linear model given by

$$\mathbf{z}_{\text{exp}} = \mathbf{z}_{\text{disc}}(\boldsymbol{\theta}) + \boldsymbol{\epsilon}_{\text{disc}}, \quad (9)$$

where $\mathbf{z}_{\text{disc}}(\boldsymbol{\theta}) \in \mathbb{R}^{2N}$ is the concatenated vector of real and imaginary discrete model impedance values, $\boldsymbol{\theta} \in \mathbb{R}^{2+4Q}$ is the vector of discrete model parameters, and $\boldsymbol{\epsilon}_{\text{disc}} \in \mathbb{R}^{2N}$ is the vector of discrete model errors. However, fitting discrete element models to impedance data is a non-linear optimization problem that contains many local minima. The fitting process is often slow, scales poorly as the number of elements increases, and has a substantial risk of converging to a suboptimal solution [21]. Models constructed from HN elements are particularly challenging due to the large number of parameters per element and the interaction between symmetry and dispersion parameters. Since our framework considers multiple candidate models for a single spectrum, some of which may contain a large number of elements, it is essential to develop an efficient, reliable method for discrete model optimization. To do so, we apply several enhancements to the “naive” equivalent circuit model optimization method:

1. Estimate and initialize parameter values from the DRT.
2. Transform and scale parameters for favorable optimization geometry.
3. Apply priors and bounds to parameter values.
4. Automatically construct an analytical expression for the Jacobian matrix.

The details of these modifications are provided in Section S2.2. While parameter estimation from the DRT is a common practice for initializing equivalent circuit models from DRT estimates [2,4,5,11] and analytical Jacobian matrices are employed in some equivalent circuit fitting packages [32,33], the application of priors and parameter transformations seems to be less commonly discussed. The enhanced optimization procedure enables reliable convergence with an order of magnitude decrease in run time relative to the base optimization procedure.

2.1.4. Model selection

In order to select the most suitable model from the candidates generated as described in the preceding sections, we must define criteria for evaluation and comparison of models. The criteria must balance the model complexity, defined by the number of peaks Q , with its ability to explain the data. Since the goodness of fit of the continuous DRT candidates is strongly influenced by the smoothing regularization, we focus instead on their discrete counterparts. We consider two criteria that arise from Bayesian statistics – the Bayesian information criterion and the model evidence – and apply them to the generated candidate discrete models. Identifying the most suitable model via these criteria solves the regression and classification problems by predicting both the overall DRT and its constituent relaxations. In addition, the consideration and credibility quantification of multiple candidate models provides crucial and meaningful insight into uncertainty in EIS analysis.

We also introduce the *probability function of relaxation times*, which ranks the plausibilities of the individual peaks under consideration. The probability function of relaxation times is the pure-classification counterpart to the DRT: it directly completes the classification objective by predicting the presence of relaxations without explicitly addressing the regression objective.

Bayesian information criterion. The Bayesian information criterion (BIC) is a criterion that can be applied to compare a finite set of models. For a discrete model with Q elements, the BIC is defined as [34]

$$\text{BIC}(Q) = K \ln N - 2 \ln \hat{\mathcal{L}}(Q), \quad (10)$$

where $K = 2 + 4Q$ is the number of free parameters in the model, N is the number of data points, and $\ln \hat{\mathcal{L}}(Q)$ is the optimal (maximum) value of the log-likelihood for the discrete model (Equation S73). Given a choice of several models, models with lower BIC values are favored. The BIC arises from an approximation of the model evidence, discussed in the next section, but relies on a number of assumptions. In particular, the BIC assumes that $N \gg K$, which may not always be valid for impedance data and models. However, the BIC is easily calculated and widely employed, making it a good baseline metric for reference and comparison.

Model evidence. The model evidence, or marginal likelihood, is a sensitive criterion for Bayesian model selection [35]. The marginal likelihood for a discrete model Q , $p(\mathbf{z}_{\text{exp}}|Q)$, considers the likelihood function and prior over all possible values of model parameters (Equation S74), but is typically difficult to calculate and often must be approximated via costly methods like Monte Carlo sampling [35,36]. However, simpler approximations are available. As noted above, the BIC is based on an approximation of the log-marginal likelihood (LML):

$$\text{BIC} \approx -2 \ln p(\mathbf{z}_{\text{exp}}|Q). \quad (11)$$

We consider another approximate analytical expression for the LML which accounts for parameter interactions in the discrete model by applying Laplace’s method [36], derived in Section S2.4:

$$\ln p(\mathbf{z}_{\text{exp}}|Q) \approx \ln \hat{\mathcal{L}}(Q) + \ln \hat{p}(Q) - \frac{1}{2} | -2\pi \mathbf{H} |, \quad (12)$$

where $\ln \hat{\mathcal{L}}(Q)$ and $\ln \hat{p}(Q)$ are the optimized values of the log-likelihood and log-prior probability density, respectively, and \mathbf{H} is the local Hessian matrix of the log-likelihood plus the log-prior with respect to

the discrete model parameters. Throughout the remainder of the text, we refer to the approximate LML in Eq. (12) simply as the LML for brevity. While Eq. (12) is still an approximation, it relaxes several of the assumptions implicit in the BIC and thus may be more suitable for model selection in some cases. However, Eq. (12) can produce misleading results when unnecessary parameters are included in the model or the optimization converges to a suboptimal result, making the BIC a more reliable criterion in general. However, further methods for estimating the LML should be explored to improve upon the BIC.

Probabilistic model comparison. Either the BIC or the LML can be used to estimate the relative probabilities of different discrete models. When comparing two models Q_1 and Q_2 , the ratio of their marginal likelihoods quantifies their relative plausibilities [36]:

$$B_{Q_1 Q_2} = \frac{p(\mathbf{z}_{\text{exp}} | Q_1)}{p(\mathbf{z}_{\text{exp}} | Q_2)} \approx \exp \left(\frac{\text{BIC}_2 - \text{BIC}_1}{2} \right). \quad (13)$$

The ratio $B_{Q_1 Q_2}$ is known as the Bayes factor. Given a set of candidate discrete models, we can compute the Bayes factor for each model relative to the most probable model. These normalized Bayes factors then represent a probability distribution over models. The Bayes factors have powerful applications: they can be used not only for autonomous discrete model selection, but also to interrogate the credibility of different models when multiple models are plausible, as demonstrated in Section 3.1. We contrast this to the calculation of a credibility interval for γ_{cont} , which is the typical means for representing uncertainty in the DRT [8,16,18,19]: the continuous credible interval only tells us about possible variations in the magnitude of $\gamma_{\text{cont}}(\ln \tau)$, but does not provide direct information about the credibility of discrete models or peaks.

The probability function of relaxation times. The BIC, LML, and Bayes factors provide a means for comparing different discrete models. However, it is also informative to quantify the plausibilities of individual peaks suggested by the various models. To do so, we define the probability function of relaxation times (PFRT), $p(\ln \tau)$. Whereas the DRT quantifies the *magnitude* (resistance) of the relaxation at each $\ln \tau$, the PFRT quantifies the *probability* that a peak exists in the DRT at each $\ln \tau$. In contrast to the dispersed, overlapping peaks that are common in the DRT, the PFRT summarizes the information contained in the data as a series of well-resolved spectral lines. The PFRT also has the advantage of decoupling peak magnitude from credibility. Like the DRT, one may envision many different methods for calculating the PFRT, which may yield varying results. For example, the PFRT may be constructed from continuous DRT estimates by considering the frequency and plausibility of peak appearance in the estimates, or from discrete candidate models and their Bayes factors. The PFRTs presented in Section 3 were generated from continuous DRT estimates following the procedure described in Section S3. The PFRT provides a semi-quantitative indication of the evidence for inclusion of different candidate peaks, making it a powerful tool for model selection.

2.2. Evaluating DRT accuracy

In addition to suggesting a new way to approach the DRT inversion problem, the dual regression-classification interpretation of the DRT provides important perspective on how the accuracy of DRT algorithms should be quantified. We first define the general setting for the application of these DRT evaluation metrics. We assume that the exact DRT, $\gamma_{\text{exact}}(\ln \tau)$, is known; this is the standard case when validating DRT algorithms using simulated data. The DRT algorithm of interest is applied to noisy impedance data generated from γ_{exact} for a vector of frequencies $\omega \in \mathbb{R}^N$. To develop generalized metrics, we make no assumptions about the nature of the DRT algorithm except that it produces an estimated distribution, $\gamma_{\text{est}}(\ln \tau)$, which can be evaluated at an arbitrary set of $\ln \tau$ values. For convenience, we assume that the exact and estimated DRTs are normalized to unit polarization resistance. While unnormalized distributions may also be used in the

calculations, normalized values will produce the most consistent and comparable results.

The regression and classification views each suggest different metrics derived from the corresponding class of problem. We develop the necessary framework to apply these metrics to the DRT inversion problem in the following sections.

2.2.1. Regression view

The regression view of accuracy is concerned with the agreement between the magnitudes of the estimated and exact distributions at a finite set of $\ln \tau$ grid points. We select a log-uniform grid of evaluation time constants, $\tau_{\text{eval}} \in \mathbb{R}^M$. For notational convenience, let $\mathbf{t} = \ln(\tau_{\text{eval}})$. Then, vectors of the exact and estimated DRTs evaluated at the grid points, $\gamma_{\text{exact}}(\mathbf{t})$ and $\gamma_{\text{est}}(\mathbf{t})$, may be used to calculate regression metrics. The evaluation grid can be selected with some basic considerations (see Section S4.1).

The prototypical regression metric is the coefficient of determination, R^2 , which is given by [37]

$$R^2 = 1 - \frac{\|\gamma_{\text{exact}}(\mathbf{t}) - \gamma_{\text{est}}(\mathbf{t})\|_2^2}{\|\gamma_{\text{exact}}(\mathbf{t}) - \bar{\gamma}_{\text{exact}}(\mathbf{t})\|_2^2}, \quad (14)$$

where $\bar{\gamma}_{\text{exact}}(\mathbf{t})$ is the mean of the exact DRT over \mathbf{t} . The numerator of the ratio on the right-hand side of Eq. (14) is the sum of squared residuals, while the denominator is proportional to the sample variance. The ratio can be interpreted as the fraction of the variance of γ_{exact} that is *not* explained by γ_{est} , while R^2 is the fraction of the variance that is explained by γ_{est} . The optimal value of R^2 is 1, while a value of 0 indicates that γ_{est} is no better a predictor of γ_{exact} than $\bar{\gamma}_{\text{exact}}$.¹ Ciucci and Chen previously applied the unexplained fraction of variance ($1 - R^2$) to evaluate the accuracy of DRT algorithms [10]. To the best of our knowledge, this is the only quantitative evaluation metric that has been applied to DRT accuracy in the literature.

A concept that is closely related to but not directly derived from the regression view is divergence, which is a statistical distance between two probability distributions [38]. Although the normalized DRT is not strictly a probability distribution, its similarity to a one-dimensional continuous probability distribution suggests that divergence may be useful for quantifying discrepancies between DRTs. Because this is not a stringent statistical application of divergence, the divergence values computed for DRT comparisons should be considered pseudo-divergences, which are not guaranteed to hold all the same properties as strict statistical divergences. We consider several types of divergence: the squared Euclidean distance (SED), the Kullback–Leibler divergence (KLD), and the Jensen–Shannon divergence (JSD). While the SED (Equation S83) is relatively uninformative as a metric, its close relationship to R^2 establishes a clear link between divergence and the regression view. The KLD is based on the concept of entropy rather than Euclidean distance and is given by [39]

$$D_{\text{KL}}(\gamma_{\text{exact}} \parallel \gamma_{\text{est}}) = \int_{-\infty}^{\infty} \gamma_{\text{exact}}(t) \cdot \ln \left(\frac{\gamma_{\text{exact}}(t)}{\gamma_{\text{est}}(t)} \right) dt. \quad (15)$$

The quantity $D_{\text{KL}}(\gamma_{\text{exact}} \parallel \gamma_{\text{est}})$ can be interpreted as the amount of information that is lost when γ_{est} is used to approximate γ_{exact} [40]. The JSD is a symmetrized version of the KLD and is given by [41]

$$D_{\text{JS}}(\gamma_{\text{exact}}, \gamma_{\text{est}}) = \frac{1}{2} (D_{\text{KL}}(\gamma_{\text{exact}} \parallel \tilde{\gamma}) + D_{\text{KL}}(\gamma_{\text{est}} \parallel \tilde{\gamma})), \quad (16)$$

where $\tilde{\gamma} = (\gamma_{\text{exact}} + \gamma_{\text{est}})/2$. The divergence integrals may be evaluated numerically using the same grid of evaluation points \mathbf{t} as for R^2 .²

¹ Although negative values of R^2 are possible, the risk of obtaining $R^2 < 0$ is relatively low in the context of practical application of the DRT.

² Note that if $\gamma_{\text{est}}(t) = 0$ and $\gamma_{\text{exact}}(t) \neq 0$ for any $t \in \mathbf{t}$, the KLD becomes infinite. To avoid this issue, we pad both distributions with a small constant value of 10^{-5} for calculation of the KLD and JSD, which is sufficient to prevent infinite divergences without significantly affecting the features of the distributions.

The metrics defined here assume that both γ_{exact} and γ_{est} are finite for all $\ln \tau$. However, the DRTs of some commonly used equivalent circuit elements, such as RC and Gerischer elements, contain singularities (points at which the DRT approaches infinity). This will result in infinite or undefined values if the metrics are evaluated directly. To avoid this issue, we suggest discretizing any DRT which contains a singularity into a relaxation mass function (analogous to a probability mass function), as described in Section S4.1.1.

2.2.2. Classification view

To the best of our knowledge, all DRT evaluation metrics proposed to date apply the regression view. While this view quantifies how closely the magnitude of the estimate matches the exact distribution at different timescales, it ignores both the nature of the underlying generative processes and our interpretation of the DRT. To capture these aspects, we suggest incorporating metrics derived from classification problems. While the regression view of DRT estimation is fairly intuitive and leads to straightforward definition of metrics, the classification view is less obvious and requires substantial definition and development to enable calculation of metrics. In this section, we provide the conceptual framework to treat the DRT inversion problem as a classification task and calculate several common classification metrics. The mathematical details of the approach are provided in Section S4.2.

For the evaluation of DRT classification accuracy, we suggest treating the DRT inversion as a binary pseudo-classification task. In the standard binary classification setting, we are given a finite set of observations and asked to assign each observation to one of two categories (positive or negative). We can think of the DRT inversion in a similar manner: we must predict where there are peaks in the DRT and where there are not. However, this problem does not translate directly to the classification setting, as there are an infinite number of time constants at which a peak might be located, and there is no restriction on how close two peaks may be to each other. Nonetheless, we can proceed by representing peaks in the exact and estimated DRT as positives, with the absence of peaks represented as negatives. It is immediately clear that while positives are well-defined and finite in number, negatives are ill-defined, since there are an infinite number of $\ln \tau$ locations at which no peak is present and therefore an infinite number of negatives. With this in mind, we adapt the definitions of the following sets from binary classification [42]:

- Positives (P): peaks in the exact DRT (“real peaks”)
- Negatives (N): peak absences in the exact DRT; ill-defined
- Predicted positives (PP): peaks in the estimated DRT (“predicted peaks”)
- Predicted negatives (PN): peak absences in the estimated DRT; ill-defined
- True positives (TP): acceptable matches between real peaks and predicted peaks: $TP = P \cap PP$
- False positives (FP): predicted peaks with no acceptable matching real peak: $FP = PP \setminus P$ (\setminus is the set difference operator)
- True negatives (TN): acceptable matches between peak absences in the exact DRT and peak absences in the estimated DRT; ill-defined
- False negatives (FN): real peaks with no acceptable matching predicted peak: $FN = P \setminus PP$

The cardinalities (number of elements) of the sets defined above are the basis for many classification metrics. While negatives (N), predicted negatives (PN), and true negatives (TN) cannot be clearly defined, several useful metrics can be calculated without these quantities.

To identify the sets defined above, we apply the following procedure to the exact and estimated DRTs:

1. Identify peaks in the exact and estimated DRTs (real peaks and predicted peaks, respectively).

2. Match predicted peaks to real peaks.

3. Determine the correctness of each match and assign fractional true (correct) and false (incorrect) character to each match accordingly.

4. Assign all unmatched peaks full false (incorrect) character.

The details of the procedure are given in Section S4.2. This process produces pseudo-counts of the number of true positives (N_{TP}), false positives (N_{FP}), and false negatives (N_{FN}) for a given γ_{exact} and γ_{est} (Equations S92–S94).

The pseudo-counts obtained from the peak-matching process enable the calculation of several classification metrics [42]. The true positive rate (TPR), also known as the sensitivity or recall, quantifies how sensitive the DRT algorithm is to the presence of real peaks:

$$\text{TPR} = \frac{N_{TP}}{N_{TP} + N_{FN}} = \frac{N_{TP}}{|P|}. \quad (17)$$

The positive predictive value (PPV), also known as the precision, quantifies how often predicted peaks indicate the presence of real peaks:

$$\text{PPV} = \frac{N_{TP}}{N_{TP} + N_{FP}} = \frac{N_{TP}}{|PP|}. \quad (18)$$

Although the TPR and PPV both place N_{TP} in the numerator, they evaluate different, often contradictory, properties of an algorithm. A sensitive algorithm (high TPR) may predict every real peak but also predict many false peaks, resulting in a low PPV. In contrast, a precise algorithm (high PPV) may not predict any false peaks, but it may also fail to identify a large fraction of real peaks, resulting in a low TPR. Since both precision and sensitivity are required for accurate peak identification, we also consider two metrics that combine the TPR and PPV. The first is the F-score, which is the harmonic mean of the TPR and PPV [42]:

$$F_1 = 2 \frac{\text{TPR} \cdot \text{PPV}}{\text{TPR} + \text{PPV}}. \quad (19)$$

The second is the Fowlkes–Mallows Index (FMI) [43], which is the geometric mean of the TPR and PPV:

$$\text{FMI} = \sqrt{\text{TPR} \cdot \text{PPV}}. \quad (20)$$

While both metrics incorporate the TPR and the PPV, the harmonic and geometric means have different properties and lead to slightly different interpretations, as discussed in Section 2.2.3.

Precision-recall curves. Conventional binary classification models typically predict the *probability* that a sample belongs to the positive category. This results in different PPV and TPR values depending on the choice of probability threshold that determines whether each sample is assigned to the positive or negative class [42,44]. Precision-recall (i.e. PPV-TPR) curves are used to evaluate the skill of binary classifiers across all threshold values. Although DRT algorithms are fundamentally different from conventional classifiers, the concept of the precision–recall curve can be applied and enhanced with regression metrics to provide additional insight into the performance of DRT estimators, as illustrated in Section S4.3. The regression-enhanced precision–recall curve separates the influence of the model regularization scheme from the hyperparameter tuning method, making it a useful tool for designing DRT algorithms.

2.2.3. Combining metrics: indices

It is sometimes useful to combine metrics to produce a new metric that represents, in a single value, all of the properties measured by its constituents. A metric produced in this way is known as an *index* [45]. The F-score and FMI (Eqs. (19) and (20)) are two examples of indices that attempt to represent the predictive accuracy of a classifier. The difference is in how they combine the TPR and PPV: the F-score is the harmonic mean, while the FMI is the geometric mean. The geometric mean is simple to interpret; it represents the multiplicative midpoint of

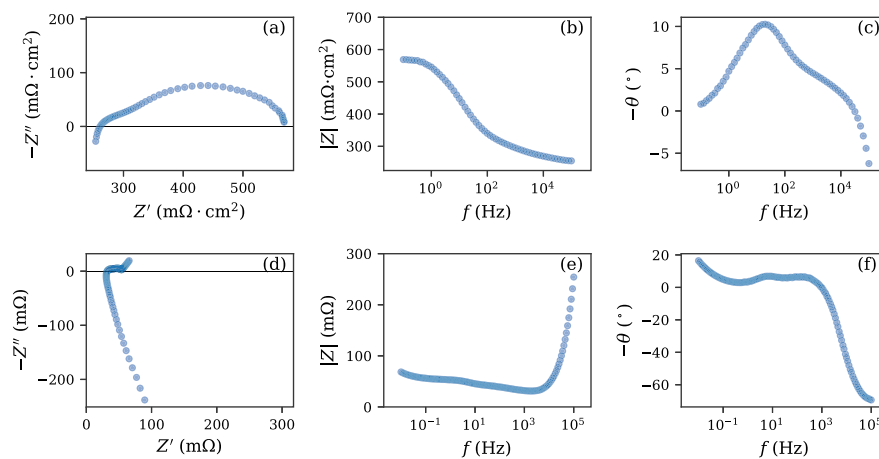


Fig. 2. Experimental impedance spectra. (a–c): Nyquist plot (a) and Bode modulus (b) and phase (c) plots of the PCFC impedance. (d–f): Nyquist plot (d) and Bode modulus (e) and phase (f) plots of the LIB impedance.

the two values, with both values receiving equal weight. The behavior of the harmonic mean is somewhat different and may be interpreted in terms of a circuit analog. Consider the constituent metrics to represent resistors in parallel. When one resistance is much smaller than the other, the vast majority of the current will flow through the smaller resistor and the total resistance of the circuit will be approximately equal to the smaller resistance. When the two resistances are similar in value, both resistors will contribute roughly equally to the total resistance. Returning to the context of combination metrics, when one metric is much smaller (worse) than the other, it will dominate the harmonic mean, dramatically lowering the value of the index. When the two metrics are similar in value, they contribute roughly equally, and the harmonic mean approaches the geometric mean. The harmonic mean is always less than or equal to the geometric mean. Thus, a geometric mean index can be viewed as representing the average performance across the categories considered, whereas a harmonic mean index is biased towards the worst-case performance in the categories considered. Several indices combining the regression and classification views are proposed in Section 3.2.

2.3. Impedance data simulation and collection

To demonstrate the inversion and evaluation applications of the dual framework, we employ both synthetic and experimental EIS data. Synthetic spectra are crucial to validate the accuracy of DRT estimation algorithms because the true DRT is known, and can thus be compared to the estimated DRT. However, real spectra present many difficulties that are not present in simulated spectra, such as systematic errors and relaxations that have more complex forms than common circuit analogs. Thus, even though the ground truth is unknown when examining experimental spectra, it is important to demonstrate the applicability of any DRT algorithm to both synthetic and real spectra.

We generate synthetic data from several equivalent circuit analogs. We consider four circuits: an RC element in series with a ZARC element (RC-RQ), two ZARC elements in series (RQ-RQ), a Gerischer element, and three overlapping HN elements (3-HN). Each circuit also contains a series ohmic resistance and inductance, which make no contribution to the DRT. The analytical expressions for the impedance and DRT of the RC, ZARC, and Gerischer elements are provided in Section S5. The circuit parameters used for each circuit model are given in Section S7. For each circuit, the exact impedance was calculated for frequencies ranging from 100 mHz to 1 MHz with a density of 10 ppd. Heteroscedastic artificial noise was then added to the exact impedance. The scale of the errors, σ_z , is assumed to consist of a uniform resolution

component and a varying component proportional to the modulus of the impedance:

$$\sigma_z(\omega) = \sigma_{z,0} + \alpha_z |z(\omega)|, \quad (21)$$

where $\sigma_{z,0}$ is the uniform component and α_z is the proportionality factor. This error structure is both more realistic and more challenging for deconvolution than uniform errors [18, 46, 47]. The real and imaginary error scales are assumed to be equal. For the illustrative analyses presented in Sections 3.1 and 3.2, we set $\sigma_{z,0} = 0.0005 R_p$ and α_z such that the mean of $\sigma_z(\omega)$ is 0.5% of the polarization resistance, representing a moderate amount of noise. Normally distributed impedance errors were then drawn from the error structure and added to the exact impedance. The exact DRTs and noisy simulated impedance spectra for the four circuits are shown in Figure S3. In Section 3.3, we provide a systematic analysis of synthetic spectra using the same error structure but varying signal-to-noise ratios to examine the influence of noise. The RC element in the RC-RQ circuit and the Gerischer element induce singularities in the corresponding DRTs, so we discretize γ_{exact} and γ_{est} for these circuits with a grid spacing of 10 ppd to enable calculation of regression metrics. The resulting relaxation mass functions are shown in Figure S4.

We also use experimental impedance spectra obtained from a protonic ceramic fuel cell (PCFC) and a commercial lithium-ion battery (LIB) to demonstrate the practical application of the dual inversion framework. The PCFC comprises a $\text{BaCe}_{0.4}\text{Zr}_{0.4}\text{Y}_{0.1}\text{Yb}_{0.1}\text{O}_{3-\delta}$ (BCZYYb4411) electrolyte [48] with a composite NiO-BCZYYb4411 anode and a $\text{BaCo}_{0.4}\text{Fe}_{0.4}\text{Zr}_{0.1}\text{Y}_{0.1}\text{O}_{3-\delta}$ (BCFZY) cathode [49]. During the EIS measurement, the cell was held at 550 °C while dry hydrogen gas and humidified air were supplied to the anode and cathode, respectively. The EIS measurement was performed potentiostatically at open circuit voltage with an AC root-mean-square excitation amplitude of 10 mV from 100 mHz to 100 kHz with 10 ppd using a Gamry Interface 1000 potentiostat. The measured spectrum is shown in Fig. 2a–c. The LIB is a Molicel INR-18650-M35 A cell, which was characterized at room temperature at 100% state-of-charge. The EIS measurement was performed galvanostatically with zero DC current and an AC root-mean-square excitation amplitude of 125 mA from 10 mHz to 100 kHz with 20 ppd using a Gamry Interface 1010E potentiostat. The measured spectrum is shown in Fig. 2d–f.

3. Results and discussion

In this section, we demonstrate the philosophy and utility of the dual continuous-discrete framework. Section 3.1 presents results from the dual inversion algorithm, while Section 3.2 demonstrates the application of the evaluation metrics. Finally, Section 3.3 applies the framework to illustrate an exemplary approach to systematic validation of DRT algorithms, which highlights the utility of both the dual inversion algorithm and the evaluation metrics.

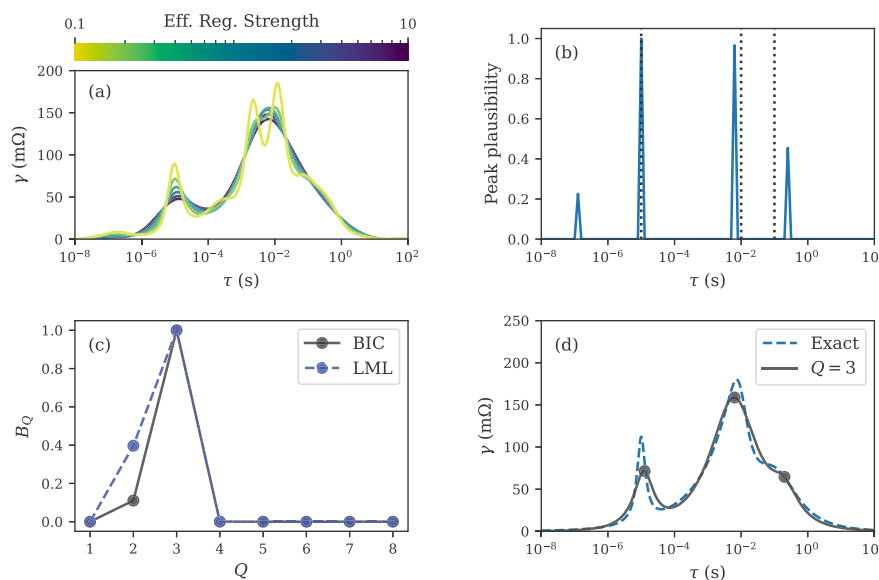


Fig. 3. Results of applying the dual inversion algorithm to the 3-HN circuit. (a) A subset of continuous candidates generated by the algorithm, each representing a different effective regularization strength as indicated by line color. The number of apparent peaks increases as the regularization strength decreases. (b) The PFRT generated from the continuous candidates indicates the relative plausibility of the presence of peaks in different locations. The locations of real peaks in the exact DRT are indicated by black dotted vertical lines. The plausibility of all three real peaks is substantially higher than the plausibility of the false peak at $\tau \approx 10^{-7}$ s. Due to overlapping relaxations and the use of local curvature minima to identify peak locations, the predicted peak locations are slightly offset from the true peak locations. (c) The normalized Bayes factors obtained from the BIC and LML for each discrete model suggest that the three-element model is most plausible, while the two-element model is less probable but possibly suitable. (d) The DRT of the optimized discrete model with three elements, overlaid with the exact DRT. Peaks in the discrete model DRT are indicated by circular markers. The exact DRT is well-represented by the discrete model.

3.1. Dual inversion framework

3.1.1. Illustration: 3-HN circuit

To illustrate the operating principles of the dual inversion framework, we first apply it to the 3-HN circuit. The exact DRT of the 3-HN circuit exhibits some of the complicating characteristics often observed in experimental systems: dispersed, overlapping peaks of varying shape and spread. The dual algorithm begins by varying the regularization hyperparameters of the continuous DRT algorithm to generate continuous candidate solutions, shown in Fig. 3a. The variation in the candidate solutions illustrates the challenge of interpreting conventional DRT results. Depending on the regularization strength, anywhere from one to seven distinct peaks may appear in the continuous DRT. Since the correct choice of tuning hyperparameters is never known with certainty in practice, this results in a high degree of ambiguity when attempting to determine the true peak locations and assign physical meaning to the DRT. The continuous candidates also highlight the complexity-smoothness correlation that is forced by smoothing regularization: as the number of peaks decreases, so does the sharpness of the peaks. This systematic over-smoothing of the simplest continuous candidates results in depressed log-likelihoods for candidates with fewer peaks (Table S6).

Recognizing the uncertainty inherent to the continuous DRT estimates, we summarize the information contained in the candidate solutions with the PFRT, shown in Fig. 3b. The PFRT provides a semi-quantitative indication of the relative plausibilities of the possible peaks suggested by the continuous candidates. The PFRT indicates that the two clearly resolved real peaks at $\tau = 10^{-5}$ s and $\tau = 10^{-2}$ s are highly probable, while the real shoulder peak at $\tau = 10^{-1}$ s is plausible, but less certain due to its overlap with the peak at $\tau = 10^{-2}$ s and the substantial noise in the data. Meanwhile, one false peak appears at $\tau \approx 10^{-7}$ s with substantially lower credibility. Thus, the PFRT provides a direct means of ranking individual candidate peaks and separating real peaks from pseudo-peaks.

While the PFRT produces a useful peak ranking, it is influenced by the smoothing regularization applied to the continuous candidates, which can obscure the true magnitudes of the peak probabilities.

Converting the continuous solutions to discrete models releases the smoothness constraint, allowing sharper peaks and better fits with simpler models, as shown in Figure S5 and Table S6. This allows full quantitative analysis of the credibility of each discrete model using the normalized Bayes factors obtained from the BIC and LML, shown in Fig. 3c. Both the BIC and LML indicate that the evidence is strongest for the three-element model, which is an accurate reproduction of the exact DRT (Fig. 3d), especially given the degree of dispersion and noise. However, both the BIC and LML also indicate that the two-element model is possible, though less plausible, and cannot be entirely discounted based on this single spectrum. This makes intuitive sense because the second and third peaks in the exact DRT overlap strongly and the amount of noise in the simulated data is substantial. This expression of uncertainty in model selection is an important feature of the dual inversion framework: even though the three-element model is the correct model, there is insufficient evidence in the simulated impedance spectrum to reject outright a simpler model for the data. Meanwhile, all other models are strongly rejected: the one-element model clearly does not capture the features of the data, whereas the marginal improvement in goodness of fit for models with four or more elements is insufficient to justify the increase in complexity. The BIC and LML are in good agreement with regard to the ranking of the candidate models, but the LML indicates slightly greater plausibility of the two-element model and lower plausibility of more complex models (Table S6).

This example illustrates the power of the dual inversion framework to not only clarify the model selection process, but to meaningfully express uncertainty in the interpretation of the DRT. Instead of producing a single DRT estimate with poorly resolved and/or erroneous peaks, which in turn is based on an uncertain choice of hyperparameters, the dual inversion provides a set of clearly defined models, possible peak locations, and corresponding quantification of credibility. Both the PFRT and the normalized Bayes factors provide insight into uncertainty in DRT interpretation and model selection. In practice, uncertainty in the interpretation of EIS data is inevitable, making the dual inversion framework a valuable tool for estimating and representing that ambiguity.

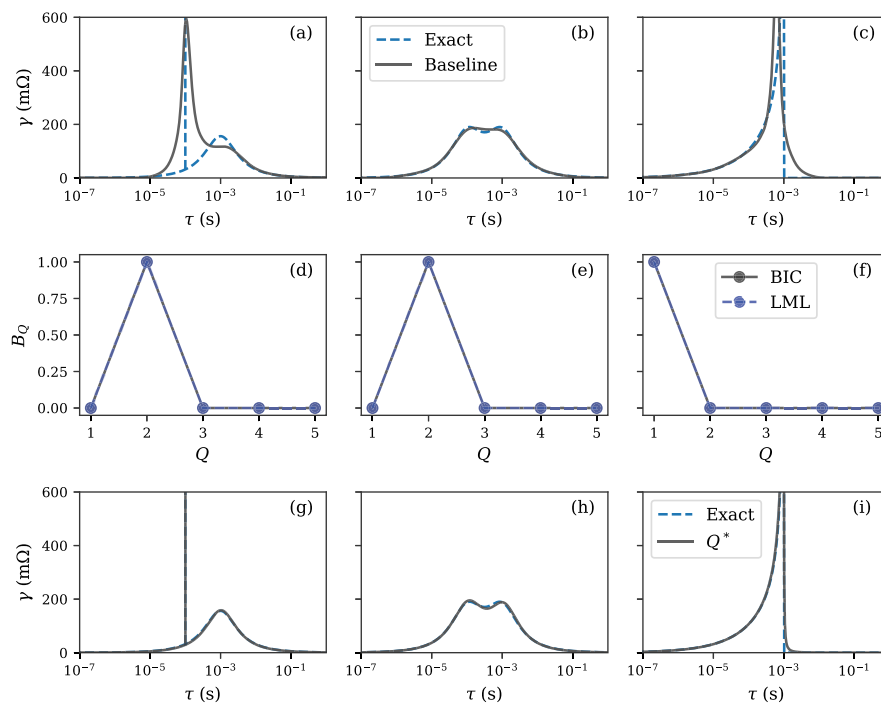


Fig. 4. Results of applying the dual inversion algorithm to the RC-RQ (left column), RQ-RQ (middle column), and Gerischer (right column) circuits. The top row of subplots (a–c) shows the baseline continuous DRT overlaid with the exact DRT for each circuit. The middle row (d–f) shows the normalized Bayes factors for the discrete model candidates generated for each circuit. The bottom row (g–i) shows the DRT of the most plausible discrete model (Q^*) overlaid with the exact DRT for each circuit. In all cases, the normalized Bayes factors select the correct number of elements, and the selected discrete model matches the exact DRT nearly perfectly.

Table 1

Computation time required to apply the dual inversion algorithm to the 3-HN circuit. The mean and standard deviation for 70 repetitions of each step are reported. The computation was performed on an HP Elitebook 840 laptop with an Intel Core i5-6300U processor and 16 GB of RAM.

Step	Run time (ms)
Baseline continuous fit	52 ± 6
Continuous candidate generation	302 ± 44
Discrete model creation	288 ± 29
Total	642 ± 53

Algorithm speed. The dual inversion algorithm requires repeated optimizations of both continuous and discrete models. During application to the 3-HN circuit, the procedure generates 42 continuous candidates, which produce seven unique discrete models containing 6–30 parameters (1–7 HN elements). However, the algorithm proceeds quickly due to the use of efficient quadratic programming methods for the continuous DRT and an enhanced nonlinear optimization procedure for the discrete models. The run time of each step is summarized in Table 1. The entire procedure requires less than one second, making it competitive with conventional DRT algorithms.

3.1.2. Further validation: simple circuits

To further validate the dual inversion framework, we apply it to the RC-RQ, RQ-RQ, and Gerischer circuits, which represent cases that have previously been used to test the performance of DRT algorithms [8,16–18]. Each circuit presents a different challenge: the RC-RQ circuit tests the model's ability to represent sharp and smooth peaks simultaneously, the RQ-RQ circuit requires deconvolution of strongly overlapping peaks, and the Gerischer element requires reconstruction of a long, smooth tail followed by a discontinuous drop.

Fig. 4 summarizes the results of applying the dual inversion algorithm to the circuits. We begin by considering the baseline continuous DRT estimates produced by the dual inversion algorithm, shown in Fig. 4a–c, which represents the behavior of a well-tuned conventional

DRT algorithm. While the baseline estimates are reasonable reproductions of the exact DRT in all cases, they contain features that could make interpretation difficult. The baseline estimate of the RC-RQ DRT slightly misplaces the ZARC peak and overestimates the degree of dispersion of the RC element (Fig. 4a). The baseline fit of the RQ-RQ circuit contains a plateau, rather than two resolved peaks (Fig. 4b). The Gerischer baseline DRT does not fully capture the asymmetry of the peak, shifts the peak position, and contains a slight hump on the left side of the peak which could be interpreted as a shoulder peak (Fig. 4c). However, the dual framework resolves these issues by exploring the space of candidate solutions and creating discrete models. In all cases, the normalized Bayes factors unequivocally select the correct model (Fig. 4d–f) and the optimized discrete models match the exact DRTs nearly perfectly for all circuits (Fig. 4g–i).

3.1.3. Practical application: experimental data

The results presented for simulated data may appear trivial because the HN element employed in the dual algorithm is a generalization of the circuit elements used in the validation circuits. However, since the HN element is based on both theory and empirical evidence, it is reasonable to expect that experimental data may contain similar features, making HN elements a practical choice for analysis of real data. We demonstrate this by applying the dual inversion algorithm to experimental data obtained from a PCFC and a LIB. The impedance spectra of PCFCs and high-temperature solid oxide fuel cells are known to contain many dispersed and overlapping features [1,3,50,51]. Models for such devices are often developed empirically, as the use of different materials and processing techniques can result in widely varying impedance spectra. Meanwhile, LIB spectra often contain high-frequency resistive-inductive relaxations and low-frequency transport processes that are described by complicated DRTs [7,52–54]. These complexities make experimental PCFC and LIB data ideal for testing the practical utility of the dual inversion framework.

To contrast the operation of the dual inversion framework with conventional DRT algorithms, we apply two existing inversion methods

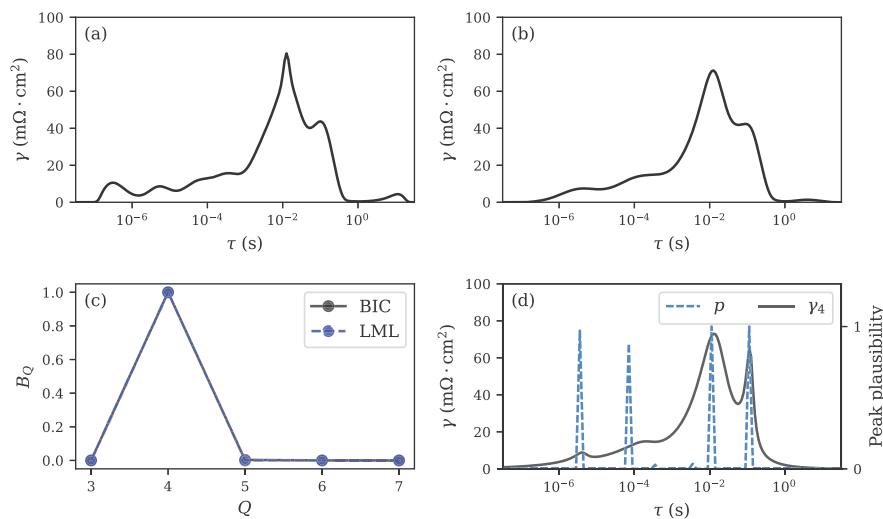


Fig. 5. Results of applying several DRT algorithms to PCFC data. (a, b) DRT estimates produced by the HL and CHB algorithms, respectively, suggest varying peak locations. (c) Normalized Bayes factors for the discrete candidates generated by the dual inversion algorithm suggest that the four-element model is most plausible. (d) The PFRT (p) generated by the dual algorithm and the DRT of the four-element discrete candidate (y_4) selected by the normalized Bayes factors. The PFRT indicates that all peaks contained in the four-element model are highly plausible, while additional peaks are relatively unlikely.

to the PCFC dataset. The first algorithm is the hyper- λ algorithm developed by Ciucci and Chen [10], which applies hierarchical regularization to the curvature of the solution and tunes the global regularization strength via real-imaginary cross-validation. The second algorithm is the hierarchical Bayesian regression model with non-linear optimization developed by Huang, Papac, and O’Hayre [18], which applies a regularization and tuning scheme similar to the ridge regression model used in the dual algorithm. These procedures are referred to as the hyper- λ (HL) and calibrated hierarchical Bayesian (CHB) algorithms, respectively, in the remainder of the text.

Fig. 5a and 5b show the PCFC DRT estimates produced by the HL and CHB algorithms, respectively. The HL algorithm requires the selection of a second tuning hyperparameter, f_β , which determines the flexibility of the hierarchical prior. We select $f_\beta = 1$ subjectively, as it suppresses additional peaks that are likely erroneous. Nonetheless, the HL algorithm suggests that as many as seven peaks may be present. The CHB algorithm suggests a simpler interpretation with four major peaks and one minor peak that appears at very long timescales. In both cases, the estimated DRT shows significant overlap and dispersion between peaks, making interpretation challenging. The significant discrepancies between the two DRT estimates, which arise from different (subjective) choices of regularization and tuning methods, present further ambiguity. However, applying the dual inversion algorithm clarifies the analysis. The PFRT indicates that four peaks are highly credible, while two additional peaks are unlikely but possible (Fig. 5d). The normalized Bayes factors confirm that four peaks are necessary to explain the data, but reject the two low-plausibility peaks identified by the PFRT, indicating that a four-element model is most plausible (Fig. 5c). It is important to note that this simply indicates that there is insufficient evidence *in this single measurement* to support the incorporation of additional elements. Further measurements, especially under different measurement conditions, might provide convincing evidence that the five-element model is necessary to explain the data. The optimized four-element model is generally in good agreement with the CHB estimate, but rejects the pseudo-peak in the CHB DRT at $\tau \approx 1$ s (Fig. 5d). The residuals for the HL, CHB, and four-element model fits are very similar in magnitude and structure (Figure S6), supporting the conclusion that the model selected by the dual algorithm is suitable. The dual algorithm is also competitive in terms of computational cost: the HL algorithm takes ~ 7 s due primarily to the real-imaginary cross-validation procedure, the CHB algorithm requires ~ 2 s, and the dual inversion algorithm takes only ~ 1.5 s.

We next apply the dual inversion algorithm to LIB data. The LIB spectrum exhibits resistive-inductive impedance at high frequencies and Warburg-like impedance at low frequencies (Fig. 6d). The high-frequency impedance may represent a skin effect, while the low-frequency impedance likely represents transport processes [52]. Previous works have shown that resistive-inductive behavior can be described by negative DRT peaks [7,18], while the low-frequency transport impedance can be described by a series of positive DRT peaks [7, 24]. Thus, we apply the dual inversion algorithm without a non-negativity constraint to the LIB spectrum to allow both positive and negative DRT peaks to be identified. The baseline DRT estimate, shown in Fig. 6a, is dominated by a series of negative peaks at short timescales, which describe the resistive-inductive impedance, and a series of positive peaks at long timescales corresponding to the transport impedance. Three smaller positive peaks at intermediate timescales ($10^{-5} \text{ s} < \tau < 10^{-1} \text{ s}$, magnified in Fig. 6b) describe the middle portion of the EIS spectrum, which exhibits semicircles in the Nyquist plane (Fig. 6d inset). Because the large high- and low-frequency peaks dominate the DRT, the prominence threshold for peak identification is set to $0.005 R_p$ (excluding the standard deviation term defined in Section 2.1.2) to ensure that the smaller intermediate-frequency peaks are detected; this highlights the need for more robust peak-finding methods. The dual inversion algorithm identifies discrete models with five to ten elements; the seven-element model is found to be most plausible, as shown in Fig. 6c. The seven-element discrete model DRT places peaks in good agreement with the baseline DRT estimate (Fig. 6a and 6b): two negative peaks describe the high-frequency impedance, three small positive peaks describe the intermediate-frequency impedance, and two increasing positive peaks describe the low-frequency impedance. However, the shapes and positions of the discrete element peaks vary somewhat from the baseline DRT peaks. Notably, the discrete element peaks near the measurement boundaries appear at more extreme timescales, which are inaccessible to the continuous DRT due to the application of smoothing regularization, which strongly penalizes DRT peaks outside of the measured frequency/timescale range. This allows the discrete element to better describe the measured high- and low-frequency impedance, as shown by the residuals for each model (Figure S7). This example highlights the ability of the dual inversion algorithm to identify, optimize, and select very complex discrete element models efficiently (the dual inversion algorithm requires ~ 5 s for this spectrum due to the higher data density and model complexity). Nonetheless, both the baseline DRT and discrete model results are difficult to

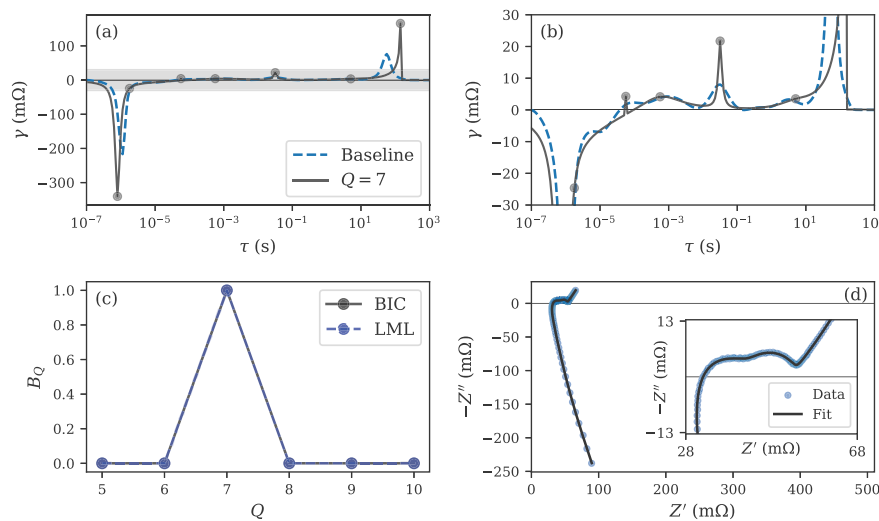


Fig. 6. Results of applying the dual inversion algorithm to LIB data. (a) DRT estimates obtained from the baseline algorithm and the most plausible discrete model with seven peaks. The circular markers indicate the discrete model peaks. The y range highlighted in gray corresponds to the region shown in (b). (b) Magnified view of the DRT estimates. (c) Normalized Bayes factors for the discrete element models identified by the dual inversion algorithm. Both BIC and LML select the seven-element model. (d) The seven-peak discrete element model fit of the EIS data. The inset shows the detail of the intermediate-frequency portion of the spectrum.

interpret in this case. Our physical understanding of the system suggests that the high- and low-frequency impedance responses each represent a single physical process, but each process is described by a series of DRT peaks. This suggests that a different model, such as the distribution of diffusion times [26], would be more suitable to treat the diverging impedance responses at the measurement boundaries. In this case, the dual inversion algorithm could be applied in a similar manner to identify and optimize distinct peaks in the distribution of diffusion times.

3.2. Dual evaluation framework

In this section, we demonstrate the dual framework for evaluation of DRT estimate accuracy. We apply the CHB and HL algorithms to generate DRT estimates with varying properties to illustrate the behavior and utility of the evaluation metrics. The HL model is more easily adjusted due to its simpler form, whereas the CHB model attempts to automatically tune a large number of hyperparameters via Bayesian inference. For this reason, the HL model is used in this section to deliberately generate suboptimal DRT estimates by manually providing hyperparameter values. Thus, the HL results shown in this section are not reflective of typical performance of the HL model.

3.2.1. Illustration: RC-RQ circuit

While regression-view metrics have been presented previously for evaluation of DRT estimates, the classification view is new to the literature and less intuitive. To clearly illustrate the classification view, we provide a demonstration of the process of constructing classification metrics for four hypothetical DRT estimates of the RC-RQ circuit. The four estimates are shown in Fig. 7 and the corresponding metrics are summarized in Table 2. Estimates I, III, and IV were obtained with the HL algorithm with manually supplied hyperparameters, while Estimate II was obtained with the CHB algorithm. Each estimate represents a different behavior: Estimate I is slightly over-regularized, Estimate II is well-tuned, Estimate III is severely over-regularized, and Estimate IV is under-regularized. Estimates I and II both predict peaks that correspond well to the real peak locations, resulting in a one-to-one matching of predicted peaks to real peaks. Since all real peaks are identified and no false peaks are predicted, Estimates I and II score very well on both TPR and PPV. Estimate III suggests that only a single broad peak exists. This predicted peak aligns reasonably well with the true location of the RC element, so it is matched to the RC peak with mostly *TP* character.

Table 2

Regression and classification metrics determined for the four DRT estimates of the RC-RQ circuit. In each column, the best value of the corresponding metric is shown in bold. While most metrics select Estimate II as the most suitable, they indicate a relatively weak preference for Estimate II over the other estimates.

Estimate	Regression metrics				Classification metrics			
	R^2	D_{KL}	D_{JS}	f_{KL}	TPR	PPV	F_1	FMI
I	0.24	0.75	0.175	0.22	0.96	0.96	0.96	0.96
II	0.45	0.48	0.131	0.38	1.00	1.00	1.00	1.00
III	0.12	1.05	0.201	0.12	0.49	0.99	0.66	0.70
IV	0.42	0.67	0.168	0.26	1.00	0.50	0.67	0.71

However, the ZARC peak in the exact DRT has no matching peak in the estimated DRT, so it is assigned full *FN* character. This results in a TPR of approximately 0.5, indicating that the predicted distribution identified only half of the real peaks. However, the PPV is nearly one, since the single estimated peak is representative of a real peak. Estimate IV contains four peaks: two of these predicted peaks match very well with the real peaks in the exact DRT, so they are assigned nearly full *TP* character. However, the remaining two predicted peaks have no matches in the exact DRT and are assigned full *FP* character. The resulting TPR is 1, since the algorithm identified every real peak; however, the PPV is only 0.5, since half of the predicted peaks are false peaks. As a result, Estimates III and IV perform very similarly on the FMI and F_1 classification indices, but for different reasons: Estimate III is precise but insensitive, whereas Estimate IV is imprecise but sensitive.

To concretely compare and contrast regression and classification metrics, we now incorporate regression metrics, summarized in Table 2, into our analysis of the RC-RQ circuit. Examining the values of the regression metrics provides several important insights. First, while all of the regression metrics identify Estimate II as the best model, Estimate IV is ranked second, whereas Estimate I is a distant third. In particular, R^2 indicates a minor difference in accuracy between Estimates II and IV despite the false peaks in Estimate IV, but a large drop in accuracy for Estimate I despite its better identification of real peaks. This highlights the limitation of regression metrics: they do not capture all aspects of the meaning and interpretation of the DRT, and therefore cannot provide a comprehensive quantification of the quality of DRT estimates. However, if we consider the classification metrics, Estimates I and II receive very similar scores, as do Estimates III and IV, in spite of the

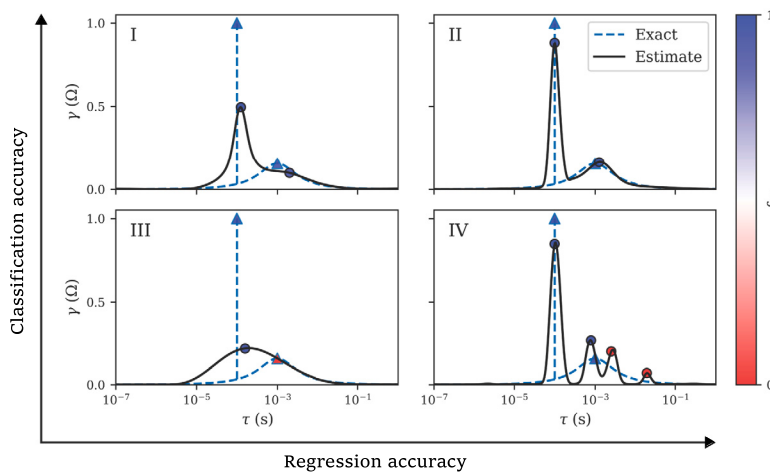


Fig. 7. Four DRT estimates obtained for the RC-RQ circuit. The number in the top left corner of each subplot corresponds to the labels given in the text. The four estimates are assigned to quadrants according to their accuracy as determined via the regression and classification interpretations of the DRT inversion. The most suitable estimate (II) is most clearly distinguished from the other estimates by the intersection of the regression and classification views. Each DRT estimate is superimposed with the exact DRT. Peaks in the exact and estimated DRTs are indicated by triangular and circular markers, respectively. The fill color of each peak marker indicates its fractional true positive character.

clear differences in regression accuracy. This reveals that classification metrics, like regression metrics, cannot be used in isolation to evaluate DRT algorithms: although they explicitly quantify correct prediction of peak locations, they tell us nothing about accurate prediction of peak shape.

The interaction of regression and classification metrics suggests the conceptual construction of four quadrants as shown in Fig. 7. Algorithms that perform well in the regression view may not perform well in the classification view, and vice versa. This indicates that a combination of metrics is necessary to fully determine the suitability of DRT algorithms. The best algorithms should exhibit strong performance in both the regression and classification views (top right quadrant). Algorithms that are accurate in one view but inaccurate in the other (top left or bottom right quadrants) may be suitable for certain applications, but should be used with caution and full awareness of their limitations.

Based on the understanding that combining regression and classification metrics provides a more complete understanding of DRT algorithm performance, we introduce several indices that attempt to summarize this insight. The indices are harmonic and geometric means of pairs of the R^2 value, KLD, F-score, and FMI. While R^2 , F-score, and FMI have maximum values of 1, the KLD ranges from 0 to infinity, with larger values indicating poorer performance. To transform the KLD to a form suitable for inclusion in the indices, we define the KLD coefficient, f_{KL} :

$$f_{KL} = e^{-2D_{KL}}. \quad (22)$$

The exponential transform results in a coefficient bounded by 0 and 1, with 1 being the optimal value. We choose a factor of 2 in the exponent because it roughly aligns the magnitude of the KLD coefficient with R^2 . The KLD coefficient values for Estimates I-IV are shown in Table 2. We can then define the following hybrid regression-classification indices:

$$h_{R^2F_1} = 2 \frac{R^2 \cdot F_1}{R^2 + F_1} \quad (23)$$

$$g_{R^2FMI} = \sqrt{R^2 \cdot FMI} \quad (24)$$

$$h_{f_{KL}F_1} = 2 \frac{f_{KL} \cdot F_1}{f_{KL} + F_1} \quad (25)$$

$$g_{f_{KL}FMI} = \sqrt{f_{KL} \cdot FMI}, \quad (26)$$

where h indices are harmonic means and g indices are geometric means.³ The geometric mean is applied to generate indices that contain

Table 3

Hybrid regression-classification indices evaluated for the four DRT estimates of the RC-RQ circuit. In each column, the best value of the corresponding index is shown in bold. All hybrid indices strongly select Estimate II.

Estimate	$h_{R^2F_1}$	g_{R^2FMI}	$h_{f_{KL}F_1}$	$g_{f_{KL}FMI}$
I	0.38	0.48	0.36	0.46
II	0.62	0.67	0.55	0.62
III	0.21	0.29	0.21	0.29
IV	0.51	0.54	0.38	0.43

a geometric mean index (the FMI), while the harmonic mean is applied to generate indices that contain a harmonic mean index (the F-score). Because each hybrid index is the mean of a regression metric and a classification index, the hybrid indices summarize combined regression and classification accuracy in a single value. The hybrid index values for the RC-RQ DRT estimates are summarized in Table 3. All of the indices show a clear preference for Estimate II and a clear rejection of Estimate III. However, the indices based on R^2 show a strong preference for Estimate IV over Estimate I, whereas the indices based on f_{KL} assign Estimates I and IV similar scores. Thus, the indices based on f_{KL} align somewhat better with our intuitive appraisal of the relative quality of the different estimates, although the R^2 -based indices could be more suitable when the absolute magnitude of the DRT is of primary interest.

3.2.2. Further validation

To further investigate the utility of different metrics and indices, we apply them to the RQ-RQ, Gerischer, and 3-HN circuits. As for the RC-RQ circuit, the HL and CHB algorithms were applied to generate four estimates for each circuit representing the same characteristic behaviors: slight over-regularization (Estimate I), appropriate regularization (Estimate II), severe over-regularization (Estimate III), and under-regularization (Estimate IV). Figures S8–S10 show the resulting DRT estimates and Tables S7–S12 summarize the corresponding metric and index values. These results reinforce the findings from the RC-RQ circuit: neither regression nor classification metrics alone are sufficient to fully distinguish different DRT estimates, but the intersection of both views elegantly captures the nuances of DRT analysis. The RQ-RQ circuit most clearly highlights the need for classification metrics (Figure S8 and Tables S7 and S8): all of the DRT estimates receive R^2 scores of at least 0.98 despite highly contrasting peak predictions. The complexity and ambiguity that can arise in practical DRT applications is perhaps best portrayed by the 3-HN circuit (Figure S9 and Tables

³ Note that if $R^2 < 0$, $h_{R^2F_1}$ will be negative and g_{R^2FMI} will be undefined.

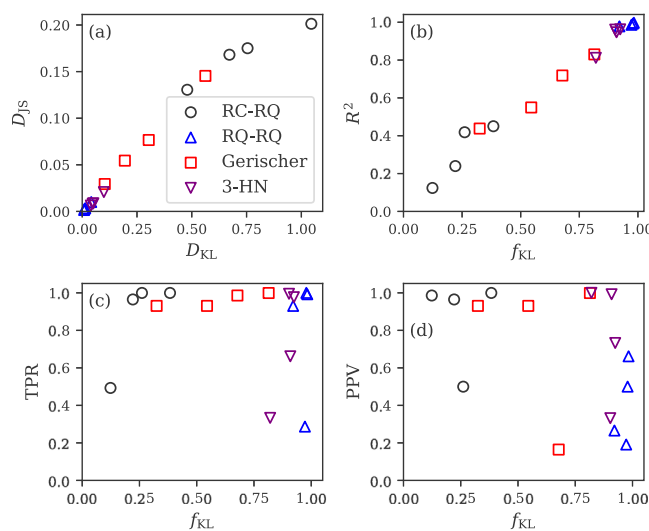


Fig. 8. Relationships between evaluation metrics for the RC-RQ, RQ-RQ, Gerischer, and 3-HN circuits: (a) D_{JS} vs. D_{KL} ; (b) R^2 vs. f_{KL} ; (c) TPR vs. f_{KL} ; and (d) PPV vs. f_{KL} . Each point represents a single DRT estimate. The marker shape and color indicate the circuit for which the estimate was obtained. While all regression metrics are strongly correlated, classification and regression metrics are uncorrelated.

S9 and S10): while several of the DRT estimates are satisfactory for regression, none are optimal for classification. However, with the aid of the metrics developed in this work, the strengths and weaknesses of a given DRT estimation algorithm can be quantified and used to inform how the algorithm is applied and analyzed. Below, we summarize the key findings from the analysis of these exemplary DRT estimates.

Within the regression view, similar trends emerge in most metrics. However, R^2 and f_{KL} (and the underlying KLD) appear to be best aligned with our intuitive assessment of DRT accuracy. The JSD produces similar results to the KLD, but appears to be less sensitive than the KLD when the discrepancy between γ_{exact} and γ_{est} is large because the JSD averages the exact and estimated distributions. Thus, we recommend R^2 and/or f_{KL} for evaluation of the regression-view accuracy of DRT estimates due to their sensitivity and interpretability. Whereas R^2 seems to favor slightly under-regularized estimates, f_{KL} appears to be more sensitive to pseudo-peaks and may favor slightly over-regularized estimates. The relationships between different regression metrics are visualized in Fig. 8a and 8b. Within the classification view, the TPR and PPV are effective for quantifying the accuracy of peak prediction in the estimated DRT. The F-score and FMI are both useful indices for quantifying the trade-off between TPR and PPV. Importantly, there is little to no correlation between regression and classification metrics (Fig. 8c and 8d). This explains why the intersection of the regression and classification views produces the most powerful metrics: the two views fundamentally measure different conceptualizations of accuracy, both of which are important in DRT estimation. The hybrid indices $g_{R^2 \text{FMI}}$, $h_{R^2 F_1}$, $g_{f_{KL} \text{FMI}}$, and $h_{f_{KL} F_1}$ summarize the information contained in both views and provide a means for unequivocally selecting the best DRT estimate with a single metric. Given the possibility of negative R^2 values and the generally good sensitivity of f_{KL} as a regression metric, we express a slight preference for $g_{f_{KL} \text{FMI}}$ and $h_{R^2 F_1}$ over the R^2 -based hybrid indices. However, the individual metrics R^2 , f_{KL} , TPR, and PPV provide independent information about different aspects of an algorithm's performance and should be considered in addition to the hybrid index values.

The evaluation metrics also highlight the benefit of the dual inversion algorithm. Figure S11 compares the values of f_{KL} and F_1 for the CHB algorithm, the baseline DRT from the dual inversion framework, and the most plausible discrete model selected by the dual inversion algorithm. While the CHB and baseline DRT estimates are well-calibrated

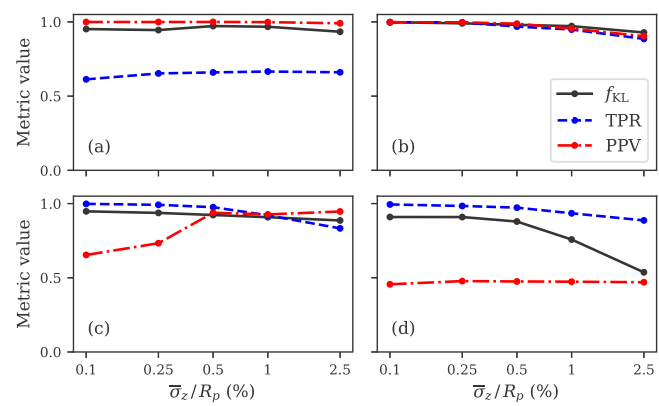


Fig. 9. Aggregated metric values evaluated for different DRT models obtained for the 3-HN circuit with varying levels of noise. The metrics in each subplot correspond to (a) the two-element discrete model optimized by the dual inversion algorithm, (b) the three-element discrete model optimized by the dual inversion algorithm, (c) the baseline continuous DRT determined by the dual inversion algorithm, and (d) the DRT estimated by the HL algorithm with real-imaginary cross-validation. The three-element discrete model exhibits the best overall performance at all noise levels, while the two-element discrete model maintains the highest precision (PPV) at high noise levels.

in the context of continuous DRT estimation, they are generally optimal for regression or classification, depending on the nature of the exact DRT, but not both. In contrast, the discrete models selected by the dual inversion algorithm are nearly ideal in both views.

3.3. Systematic DRT validation

As a final demonstration of the utility of the dual regression-classification framework, we examine the performance of different DRT algorithms as a function of signal-to-noise ratio to illustrate a systematic approach to DRT validation. The 3-HN circuit was employed to generate noisy impedance spectra using the error structure in Eq. (21) at five different mean error scales, $\bar{\sigma}_z$, ranging from 0.1% to 2.5% of the polarization resistance. At each noise level, 50 random impedance spectra were generated from the 3-HN circuit, such that a total of 250 synthetic spectra were analyzed across all signal-to-noise ratios. Figures S12a-S12c show exemplary spectra for several noise levels. The dual inversion algorithm and the HL algorithm with real-imaginary cross-validation were applied to all simulated spectra at each signal-to-noise ratio, and the resulting DRT estimates were scored using the evaluation metrics developed in this work. The dual inversion algorithm selects either the two-element or three-element discrete model as the most plausible model in nearly all cases, as discussed below. Therefore, evaluation metrics were applied to score several outputs of the dual algorithm: the continuous baseline DRT, the two-element discrete model, and the three-element discrete model. For each signal-to-noise ratio, the metrics for each model were aggregated as described in Section S4.4.

Fig. 9 compares the aggregated f_{KL} , TPR, and PPV values for each scored model as a function of signal-to-noise ratio. The two-element discrete model performs very consistently at all noise levels. Its PPV is ideal because it always identifies the presence of the two well-resolved peaks without predicting any pseudo-peaks, but its TPR is fixed at $\sim 2/3$ because it never identifies the third, poorly-resolved peak at $\tau = 10^{-1}$ s. The three-element discrete model performs nearly perfectly at low to moderate noise levels, with a slight decrease in performance at high noise levels as the large impedance errors make it difficult to accurately determine the position of the third peak. In contrast, the baseline continuous DRT exhibits consistently strong f_{KL} values but noise-dependent classification accuracy. At low noise levels, all real peaks are identified, but the data weight is high enough to consistently induce false peaks in the estimated DRT, as shown in Figure S12d,

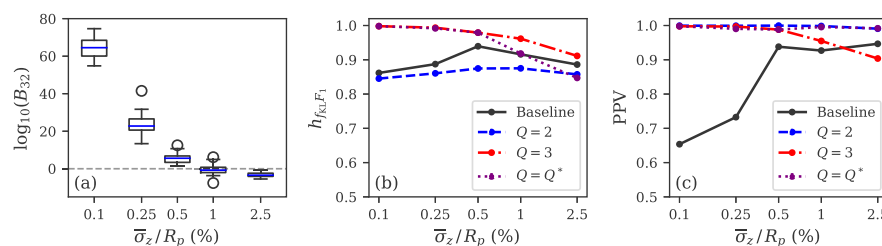


Fig. 10. Model plausibility and performance as a function of noise level for the 3-HN circuit. (a) The logarithm of the Bayes factor (evaluated with the combined LML-BIC criterion) indicating the plausibility of the three-element discrete model relative to the two-element discrete model as a function of noise level. The three-element model is more plausible at low noise levels, but the two-element model becomes increasingly plausible as the noise level increases. The blue center line in each box indicates the median value. The box extends from the first quartile to the third quartile, and the whiskers extend from the box by 1.5 times the inter-quartile range. Markers indicate any data points outside the range of the whiskers. (b, c) The aggregated value of (b) the hybrid index $h_{f_{KL}F_1}$ and (c) the PPV for each model as a function of noise level. Q^* indicates the most plausible discrete model.

resulting in ideal TPR values but lower PPV values. As the noise level increases, the strength of the data decreases, which reduces both the appearance of false peaks and the resolution of the real peaks, as illustrated by Figures S12e and S12f. The TPR falls and the PPV rises with increasing noise level as a result. The HL algorithm shows an analogous decrease in TPR with increasing noise. However, the PPV of the HL algorithm is consistently lower, indicating that false peaks are consistently present. The different behaviors of the dual algorithm baseline DRT and the HL DRT are reflective of the different prior structures and tuning methods applied.

The dual inversion algorithm identifies discrete element models with either two or three elements most frequently, although in a small number of cases it selects a model with either one or four elements, as shown in Figure S13. Based on these results, the LML and BIC appear to provide complementary information: in cases where one criterion selects the incorrect model, the other usually select the correct model. Thus, we apply the effective mean of the LML and BIC, i.e. $\frac{1}{2}(LML - BIC/2)$, as a more robust model selection criterion for this synthetic investigation. Using the combined LML-BIC criterion, the dual inversion algorithm selects discrete models with either two or three peaks for 246 of 250 spectra. Fig. 10a shows the plausibility of the three-element model relative to the two-element model as a function of the noise level. For $\bar{\sigma}_z/R_p \leq 0.5\%$, the three-element model is consistently favored. However, as the noise level increases, the poorly resolved third peak of the 3-HN circuit becomes increasingly difficult to distinguish, and the plausibility of the two-element model increases. For $\bar{\sigma}_z/R_p = 1\%$, both models are reasonably plausible, whereas for $\bar{\sigma}_z/R_p = 2.5\%$, the severe amount of noise favors the simpler two-element model. This is an important aspect of the probabilistic model selection procedure: as the evidence in the data weakens due to stronger noise, the principle of parsimony suggests that simpler models are more suitable.

Fig. 10b summarizes the performance of the baseline DRT, the two- and three-element discrete models, and the most plausible discrete model as a function of noise level with the hybrid index $h_{f_{KL}F_1}$. The three-element discrete model performs the best in all cases, followed by the continuous baseline DRT and then the two-element discrete model. As the most plausible discrete model transitions from the three-element model to the two-element model at $\bar{\sigma}_z/R_p = 1\%$, the performance of the most plausible discrete model transitions from the three-element model to the two-element model. This would suggest that using the baseline DRT might yield better accuracy (as quantified by $h_{f_{KL}F_1}$) than the most plausible discrete model at higher noise levels. However, the probabilistic discrete model selection process offers a unique benefit: the PPV of the most plausible discrete model is ≈ 1 in all cases, whereas the PPV of the continuous DRT estimates is substantially lower in virtually all cases (Fig. 10c). Thus, the discrete model selected by the dual algorithm provides a high degree of confidence in the predicted peak locations with low risk of false peaks, while the possibility of additional peaks can be examined via the PFRT and the Bayes factors of the higher-complexity candidate models. In contrast, the lower PPV

of the baseline continuous DRT estimate indicates that it consistently produces false peaks, making interpretation difficult.

This example also highlights the value of the metrics developed here: the accuracy of the 250 DRT estimates from each model across all noise levels can be comprehensively and objectively quantified with several summary metrics. Without these metrics, such a comparison would require manual and subjective examination of individual DRT estimates by an experienced DRT practitioner to determine their suitability for the application of interest.

4. Conclusions

In this work, we introduce a classification view of the DRT inversion problem and develop a framework to unite this new view with the conventional regression interpretation. The framework provides a structure for dual regression-classification DRT inversion algorithms that address several key challenges in DRT estimation, interpretation, and model selection. An exemplary dual inversion algorithm is developed and applied to simulated and experimental data, demonstrating promising efficiency, accuracy, and interpretability. Further implementations of dual inversion algorithms, which may employ different methods of continuous candidate generation and discrete model construction, should be explored. We also introduce the novel probability function of relaxation times (PFRT), which directly addresses the classification view by predicting the existence of individual relaxations. The PFRT is a powerful tool for model selection that can play a complementary role to the DRT in EIS analysis.

The framework is also applied to the problem of evaluating the accuracy of DRT algorithms. Robust metrics are developed from regression and classification views of the inversion problem and applied to DRT estimates obtained for simulated data. The R^2 , f_{KL} , TPR, and PPV metrics are shown to be sensitive indicators of different aspects of DRT accuracy. Hybrid regression-classification indices are shown to provide powerful differentiation of DRT estimates. The general evaluation framework and specific metrics developed in this work may be valuable for benchmarking the performance of DRT algorithms, designing new algorithms, and informing the interpretation of DRT estimates in practical settings.

Finally, we stress that the conceptual and mathematical framework of the dual regression-classification perspective is not confined to the particular methods developed in this work. Myriad approaches to dual inversion algorithms, PFRT estimation, and construction of accuracy metrics are possible under the framework. The probabilistic foundations of the framework may also have applications to autonomous analysis of large EIS datasets generated by exhaustive characterization under varied conditions or high-throughput experimentation: multiple measurements can be assimilated to increase confidence in peak identification and model selection.

CRediT authorship contribution statement

Jake Huang: Conceptualization, Methodology, Software, Formal analysis, Investigation, Writing – original draft. **Neal P. Sullivan:** Writing – review & editing, Funding acquisition. **Andriy Zakutayev:** Writing – review & editing, Supervision, Funding acquisition. **Ryan O'Hayre:** Writing – review & editing, Supervision, Funding acquisition.

Declaration of competing interest

The authors declare that they have no known competing financial interests or personal relationships that could have appeared to influence the work reported in this paper.

Data availability

Supporting code and data are available online (see Software availability). Additional data is available upon request.

Acknowledgments

Research supported as part of the Hydrogen in Energy and Information Sciences (HEISs) center, an Energy Frontier Research Center funded by the U.S. Department of Energy (DOE), Office of Science, Basic Energy Sciences (BES), under award No. DE-SC0023450 (methodology development, software, validation, formal analysis), by the Army Research Office (ARO) under Award No. W911NF-22-1-0273 (PCFC fabrication, electrochemical measurement station development), and by the National Renewable Energy Laboratory (NREL), under the Laboratory Directed Research and Development (LDRD) program (LIB and PCFC impedance measurement, development of automated fitting and analysis routines, visualization). NREL is a U.S. Department of Energy FFRDC, managed and operated under contract No. DEAC36-08GO28308 with the Alliance for Sustainable Energy, LLC. The views and opinions of authors expressed herein do not necessarily state or reflect those of the United States Government or any agency thereof. J.H. thanks Hilary Egan (NREL) for discussions about probabilistic interpretations of the DRT and methods for constructing the PFRT.

Software availability

To enable application and further development, a Python package implementing the methods described in this work is available at github.com/jdhuang-csm/hybrid-drt. This package makes use of several existing Python libraries for scientific data analysis [31,55–58].

Appendix A. Supplementary data

Supplementary material related to this article can be found online at <https://doi.org/10.1016/j.electacta.2023.141879>.

References

- [1] E. Ivers-Tiffée, A. Weber, Evaluation of electrochemical impedance spectra by the distribution of relaxation times, *J. Ceram. Soc. Japan* 125 (4) (2017) 193–201, <http://dx.doi.org/10.2109/jcersj2.16267>.
- [2] S. Dierickx, A. Weber, E. Ivers-Tiffée, How the distribution of relaxation times enhances complex equivalent circuit models for fuel cells, *Electrochim. Acta* 355 (2020) 136764, <http://dx.doi.org/10.1016/j.electacta.2020.136764>.
- [3] J. Xia, C. Wang, X. Wang, L. Bi, Y. Zhang, A perspective on DRT applications for the analysis of solid oxide cell electrodes, *Electrochim. Acta* 349 (2020) 136328, <http://dx.doi.org/10.1016/j.electacta.2020.136328>.
- [4] Q. Wang, Z. Hu, L. Xu, J. Li, Q. Gan, X. Du, M. Ouyang, A comparative study of equivalent circuit model and distribution of relaxation times for fuel cell impedance diagnosis, *Int. J. Energy Res.* 45 (11) (2021) 15948–15961, <http://dx.doi.org/10.1002/er.6825>.
- [5] H. Li, Z. Lyu, M. Han, Robust and fast estimation of equivalent circuit model from noisy electrochemical impedance spectra, *Electrochim. Acta* 422 (2022) 140474, <http://dx.doi.org/10.1016/j.electacta.2022.140474>.
- [6] B.A. Boukamp, A. Rolle, Analysis and application of distribution of relaxation times in solid state ionics, *Solid State Ion.* 302 (2017) 12–18, <http://dx.doi.org/10.1016/j.ssi.2016.10.009>.
- [7] M.A. Danzer, Generalized distribution of relaxation times analysis for the characterization of impedance spectra, *Batteries* 5 (3) (2019) 1–16, <http://dx.doi.org/10.3390/batteries5030053>.
- [8] S. Effendi, J. Song, M.Z. Bazant, Analysis, design, and generalization of electrochemical impedance spectroscopy (EIS) inversion algorithms, *J. Electrochem. Soc.* 167 (10) (2020) 106508, <http://dx.doi.org/10.1149/1945-7111/ab9c82>.
- [9] M. Saccoccia, T.H. Wan, C. Chen, F. Ciucci, Optimal regularization in distribution of relaxation times applied to electrochemical impedance spectroscopy: Ridge and lasso regression methods - a theoretical and experimental study, *Electrochim. Acta* 147 (2014) 470–482, <http://dx.doi.org/10.1016/J.ELECTACTA.2014.09.058>.
- [10] F. Ciucci, C. Chen, Analysis of electrochemical impedance spectroscopy data using the distribution of relaxation times: A Bayesian and hierarchical Bayesian approach, *Electrochim. Acta* 167 (2015) 439–454, <http://dx.doi.org/10.1016/j.electacta.2015.03.123>.
- [11] X. Li, M. Ahmadi, L. Collins, S.V. Kalinin, Deconvolving distribution of relaxation times, resistances and inductance from electrochemical impedance spectroscopy via statistical model selection: Exploiting structural-sparsity regularization and data-driven parameter tuning, *Electrochim. Acta* 313 (2019) 570–583, <http://dx.doi.org/10.1016/j.electacta.2019.05.010>.
- [12] B.A. Boukamp, Distribution (function) of relaxation times, successor to complex nonlinear least squares analysis of electrochemical impedance spectroscopy? *J. Phys.: Energy* 2 (4) (2020) 042001, <http://dx.doi.org/10.1088/2515-7655/ab9e0>.
- [13] T. Hörlin, Deconvolution and maximum entropy in impedance spectroscopy of noninductive systems, *Solid State Ion.* 107 (3–4) (1998) 241–253, [http://dx.doi.org/10.1016/S0167-2738\(98\)00008-3](http://dx.doi.org/10.1016/S0167-2738(98)00008-3).
- [14] B.A. Boukamp, Fourier transform distribution function of relaxation times; application and limitations, *Electrochim. Acta* 154 (2015) 35–46, <http://dx.doi.org/10.1016/j.electacta.2014.12.059>.
- [15] Y. Zhang, Y. Chen, M. Li, M. Yan, M. Ni, C. Xia, A high-precision approach to reconstruct distribution of relaxation times from electrochemical impedance spectroscopy, *J. Power Sources* 308 (2016) 1–6, <http://dx.doi.org/10.1016/j.jpowsour.2016.01.067>.
- [16] M.B. Effat, F. Ciucci, Bayesian and hierarchical Bayesian based regularization for deconvolving the distribution of relaxation times from electrochemical impedance spectroscopy data, *Electrochim. Acta* 247 (2017) 1117–1129, <http://dx.doi.org/10.1016/J.ELECTACTA.2017.07.050>.
- [17] N. Schlüter, S. Ernst, U. Schröder, Finding the optimal regularization parameter in distribution of relaxation times analysis, *ChemElectroChem* 6 (24) (2019) 6027–6037, <http://dx.doi.org/10.1002/celec.201901863>.
- [18] J. Huang, M. Papac, R. O'Hayre, Towards robust autonomous impedance spectroscopy analysis: A calibrated hierarchical Bayesian approach for electrochemical impedance spectroscopy (EIS) inversion, *Electrochim. Acta* 367 (137493) (2020) <http://dx.doi.org/10.1016/j.electacta.2020.137493>.
- [19] J. Liu, F. Ciucci, The Gaussian process distribution of relaxation times: A machine learning tool for the analysis and prediction of electrochemical impedance spectroscopy data, *Electrochim. Acta* 331 (2020) 135316, <http://dx.doi.org/10.1016/j.electacta.2019.135316>.
- [20] J. Liu, F. Ciucci, The deep-prior distribution of relaxation times, *J. Electrochem. Soc.* 167 (2) (2020) 26506, <http://dx.doi.org/10.1149/1945-7111/ab631a>.
- [21] F. Ciucci, Modeling electrochemical impedance spectroscopy, *Curr. Opin. Electrochem.* 13 (2019) 132–139, <http://dx.doi.org/10.1016/j.colelec.2018.12.003>.
- [22] R. Slodzinski, L. Hildebrand, W. Vautz, Peak detection algorithm based on second derivative properties for two dimensional ion mobility spectrometry signals, in: M. Fathi (Ed.), *Integration of Practice-Oriented Knowledge Technology: Trends and Prospectives*, Springer, Berlin, Heidelberg, 2013, pp. 341–354, http://dx.doi.org/10.1007/978-3-642-34471-8_28.
- [23] R.R. Lindner, C. Vera-Ciro, C.E. Murray, S. Stanićirović, B. Babler, C. Heiles, P. Hennebelle, W.M. Goss, J. Dickey, Autonomous Gaussian decomposition, *Astron. J.* 149 (4) (2015) <http://dx.doi.org/10.1088/0004-6256/149/4/138>.
- [24] B.A. Boukamp, Derivation of a distribution function of relaxation times for the (fractal) finite length warburg, *Electrochim. Acta* 252 (2017) 154–163, <http://dx.doi.org/10.1016/j.electacta.2017.08.154>.
- [25] A. Lasia, The origin of the constant phase element, *J. Phys. Chem. Lett.* 13 (2) (2022) 580–589, <http://dx.doi.org/10.1021/acs.jpclett.1c03782>.
- [26] J. Song, M.Z. Bazant, Electrochemical impedance imaging via the distribution of diffusion times, *Phys. Rev. Lett.* 120 (11) (2018) 116001, <http://dx.doi.org/10.1103/PhysRevLett.120.116001>.
- [27] T.H. Wan, M. Saccoccia, C. Chen, F. Ciucci, Influence of the discretization methods on the distribution of relaxation times deconvolution: Implementing radial basis functions with drttools, *Electrochim. Acta* 184 (2015) 483–499, <http://dx.doi.org/10.1016/J.ELECTACTA.2015.09.097>.
- [28] A.L. Gavriluk, D.A. Osinkin, D.I. Bronin, The use of tikhonov regularization method for calculating the distribution function of relaxation times in impedance spectroscopy, *Russ. J. Electrochem.* 53 (6) (2017) 575–588, <http://dx.doi.org/10.1134/S1023193517060040>.

- [29] N. Schlüter, S. Ernst, U. Schröder, Direct access to the optimal regularization parameter in distribution of relaxation times analysis, *ChemElectroChem* 7 (16) (2020) 3445–3458, <http://dx.doi.org/10.1002/celec.202000787>.
- [30] J. Griffé, L. Boelen, G. Burn, A.P. Cope, D.M. Owen, Topographic prominence as a method for cluster identification in single-molecule localisation data, *J. Biophotonics* 8 (11–12) (2015) 925–934.
- [31] P. Virtanen, R. Gommers, T.E. Oliphant, M. Haberland, T. Reddy, D. Cournapeau, E. Burovski, P. Peterson, W. Weckesser, J. Bright, S.J. van der Walt, M. Brett, J. Wilson, K. Jarrod Millman, N. Mayorov, A.R. Nelson, E. Jones, R. Kern, E. Larson, C.J. Carey, Í. Polat, Y. Feng, E.W. Moore, J. Vand erPlas, D. Laxalde, J. Perktold, R. Cimrman, I. Henriksen, E. Quintero, C.R. Harris, A.M. Archibald, A.H. Ribeiro, F. Pedregosa, P. van Mulbregt, S. Contributors, Scipy 1.0: Fundamental algorithms for scientific computing in python, *Nature Methods* (2020) <http://dx.doi.org/10.1038/s41592-019-0686-2>.
- [32] B.A. Boukamp, A nonlinear least squares fit procedure for analysis of immittance data of electrochemical systems, *Solid State Ion.* 20 (1) (1986) 31–44, [http://dx.doi.org/10.1016/0167-2738\(86\)90031-7](http://dx.doi.org/10.1016/0167-2738(86)90031-7).
- [33] M. Žic, S. Pereverzyev, V. Subotić, S. Pereverzyev, Adaptive multi-parameter regularization approach to construct the distribution function of relaxation times, *GEM - Int. J. Geomath.* 11 (1) (2020) 1–23, <http://dx.doi.org/10.1007/s13137-019-0138-2>.
- [34] G. Schwarz, Estimating the dimension of a model, *Ann. Statist.* 6 (2) (1978) 461–464, <http://dx.doi.org/10.1214/aos/1176344136>.
- [35] C.M. Pooley, G. Marion, Bayesian model evidence as a practical alternative to deviance information criterion, *R. Soc. Open Sci.* 5 (3) (2018) <http://dx.doi.org/10.1098/rsos.171519>.
- [36] R.E. Kass, A.E. Raftery, Bayes factors, *J. Amer. Statist. Assoc.* 90 (430) (1995) 773–795, URL <https://www.jstor.org/stable/2291091>.
- [37] N.R. Draper, H. Smith, *Applied Regression Analysis*, Vol. 326, John Wiley & Sons, 1998.
- [38] S.-i. Amari, *Information Geometry and its Applications*, Vol. 194, Springer, 2016.
- [39] S. Kullback, R.A. Leibler, On information and sufficiency, *Ann. Math. Stat.* 22 (1) (1951) 79–86.
- [40] D. Anderson, K. Burnham, *Model Selection and Multi-Model Inference*, Vol. 63, second ed., Springer-Verlag, NY, 2004, p. 10, (2020).
- [41] J. Lin, Divergence measures based on the Shannon entropy, *IEEE Trans. Inform. Theory* 37 (1) (1991) 145–151.
- [42] D.M.W. Powers, Evaluation: From precision, recall and F-factor to ROC, informedness, markedness & correlation, 2007, pp. 37–63, URL <http://arxiv.org/abs/2010.16061>.
- [43] E.B. Fowlkes, C.L. Mallows, A method for comparing two hierarchical clusterings, *J. Amer. Statist. Assoc.* 78 (383) (1983) 553–569.
- [44] C. Goutte, E. Gaussier, A probabilistic interpretation of precision, recall and F-score, with implication for evaluation, in: *European Conference on Information Retrieval*, Springer, 2005, pp. 345–359.
- [45] E.R. Babbie, *The Practice of Social Research*, Cengage learning, 2020.
- [46] M.E. Orazem, A systematic approach toward error structure identification for impedance spectroscopy, *J. Electroanal. Soc.* 572 (2) (2004) 317–327, <http://dx.doi.org/10.1016/J.JELECHEM.2003.11.059>.
- [47] J.R. Macdonald, Impedance spectroscopy: old problems and new developments, *Electrochim. Acta* 35 (10) (1990) 1483–1492, [http://dx.doi.org/10.1016/0013-4686\(90\)80002-6](http://dx.doi.org/10.1016/0013-4686(90)80002-6).
- [48] S. Choi, C.J. Kucharczyk, Y. Liang, X. Zhang, I. Takeuchi, H.I. Ji, S.M. Haile, Exceptional power density and stability at intermediate temperatures in protonic ceramic fuel cells, *Nature Energy* 3 (3) (2018) 202–210, <http://dx.doi.org/10.1038/s41560-017-0085-9>.
- [49] C. Duan, J. Tong, M. Shang, S. Nikodemski, M. Sanders, S. Ricote, A. Almansoori, R. O'Hare, Readily processed protonic ceramic fuel cells with high performance at low temperatures, *Science* 349 (6254) (2015) 1321–1326, <http://dx.doi.org/10.1126/science.aab3987>.
- [50] H. Schichlein, A.C. Müller, M. Voigts, A. Krügel, E. Ivers-Tiffée, Deconvolution of electrochemical impedance spectra for the identification of electrode reaction mechanisms in solid oxide fuel cells, *J. Appl. Electrochem.* 32 (8) (2002) 875–882, <http://dx.doi.org/10.1023/A:1020599525160>.
- [51] H. Sumi, H. Shimada, Y. Yamaguchi, Y. Mizutani, Y. Okuyama, K. Amezawa, Comparison of electrochemical impedance spectra for electrolyte-supported solid oxide fuel cells (SOFCs) and protonic ceramic fuel cells (PCFCs), *Sci. Rep.* 11 (1) (2021) 1–9, <http://dx.doi.org/10.1038/s41598-021-90211-9>.
- [52] A. Jossen, Fundamentals of battery dynamics, *J. Power Sources* 154 (2) (2006) 530–538, <http://dx.doi.org/10.1016/j.jpowsour.2005.10.041>.
- [53] C. Zou, L. Zhang, X. Hu, Z. Wang, T. Wik, M. Pecht, A review of fractional-order techniques applied to lithium-ion batteries, lead-acid batteries, and supercapacitors, *J. Power Sources* 390 (2018) 286–296, <http://dx.doi.org/10.1016/j.jpowsour.2018.04.033>.
- [54] N. Meddings, M. Heinrich, F. Overney, J.S. Lee, V. Ruiz, E. Napolitano, S. Seitz, G. Hinds, R. Raccichini, M. Gaberšček, J. Park, Application of electrochemical impedance spectroscopy to commercial li-ion cells: A review, *J. Power Sources* 480 (August) (2020) <http://dx.doi.org/10.1016/j.jpowsour.2020.228742>.
- [55] S. Van Der Walt, S.C. Colbert, G. Varoquaux, The numpy array: a structure for efficient numerical computation, *Comput. Sci. Eng.* 13 (2) (2011) 22–30, <http://dx.doi.org/10.1109/MCSE.2011.37>.
- [56] W. McKinney, Data structures for statistical computing in python, in: S. van der Walt, J. Millman (Eds.), *Proceedings of the 9th Python in Science Conference*, 2010, pp. 51–56.
- [57] J.D. Hunter, Matplotlib: A 2D graphics environment, *Comput. Sci. Eng.* 9 (3) (2007) 90–95.
- [58] M.S. Andersen, J. Dahl, L. Vandenberghe, CVXOPT: A python package for convex optimization, 2013, URL cvxopt.org.